Evaluating Zr/Rb ratios from XRF scanning as an indicator of grain-size variations of glaciomarine sediments in the Southern Ocean

Li Wu[a], David J. Wilson[b], **Rujian Wang[a*]**, Xuebo Yin[c,d], Zhihua Chen[e], Wenshen Xiao[a], Mengxue Huang[a], Wout Krijgsman[f]

a. State Key Laboratory of Marine Geology, Tongji University, Shanghai, China

b. Institute of Earth and Planetary Sciences, University College London and Birkbeck, University of London, London, UK

c. Qingdao Sparta Analysis & Test Co., Ltd. Qingdao, China

d. Institute of Oceanology, Chinese Academy of Sciences, Qingdao, China

e. First Institute of Oceanography, State Oceanic Administration, Qingdao, China

f. Department of Earth Sciences, Utrecht University, Utrecht, the Netherlands

[*]Corresponding author, E-mail: rjwang@tongji.edu.cn

Abstract

The ln(Zr/Rb) count ratio derived from X-ray fluorescence (XRF) core scanning holds potential as a high-resolution tracer for grain-size variations of glaciomarine sediments. To evaluate this approach, we conducted high-resolution grain-size measurements, together with Rb and Zr measurements by XRF core scanning and Inductively Coupled Plasma-Mass Spectrometry (ICP-MS), on a series of sediment cores from different regions of the Southern Ocean. We find that downcore changes of the ln(Zr/Rb) count ratio from XRF core scanning are consistent with Zr/Rb concentration ratios derived from ICP-MS analyses, even though Rb and Zr counts deviate significantly from concentrations due to specimen and matrix effects. The ln(Zr/Rb) count ratio displays discrepancies with the bulk mean grain-size, but correlates well with the mean grain-size of the sediment fractions that do not include unsorted coarse IRD (i.e. IRD-corrected mean grain-size). These observations are supported by evidence from a grain-size separation experiment, which indicates that Zr and Rb are concentrated in different grain-size fractions. Consistent with its lack of sensitivity to coarse grain-size fractions, the ln(Zr/Rb) ratio records similar trends to the sortable silt percent (SS%) and sortable silt mean (SSM) grain-size. Universal gradients exist in plots of ln(Zr/Rb) versus SS% (34.1), and ln(Zr/Rb) versus SSM (12.7), such that the ln(Zr/Rb) ratio provides a convenient way to estimate the magnitude of changes in SS% and SSM. Overall, our results support the use of the ln(Zr/Rb) ratio as an indicator of bottom current strength in cases where the sediment is current-sorted.

Key words: Glaciomarine sediment; Southern Ocean; Grain-size; XRF core scanning Zr/Rb; Iceberg rafted debris; Bottom currents

1 Introduction

Sediment grain-size distributions contain rich information on sedimentary provenance, transport dynamics, and post-depositional modification (e.g. Chen et al., 2006; McCave and Andrews, 2019; McCave et al., 2006; Wu et al., 2020). A range of techniques has been developed for fine sediment grain-size measurements, including Laser Particle Sizer, Sedigraph, and Coulter counter (Konert and Vandenberghe, 1997; McCave et al., 2006), enabling quantitative grain-size distribution data to be obtained. However, these techniques require well-constrained laboratory conditions and are highly time-consuming. Since studies on marine sediment cores usually require analyses on large sample sets, an ability to obtain reliable sediment grain-size information more rapidly and conveniently would be of great interest to marine sedimentologists (e.g. Liu et al., 2019). Such a capability would open up the potential for targeting long high-resolution records, as well as improving spatial coverage, leading to new insights on past sediment transport and climate dynamics over a range of timescales.

It is widely recognised that chemical elements can be preferentially enriched or depleted in specific grain-size fractions within sediments or sedimentary rocks, which is referred to as the 'grain-size effect' (Bouchez et al., 2011; Jin et al., 2006; Yang et al., 2002). In most cases, this effect is considered unfavourable for geochemical data interpretation and needs to be excluded or corrected (Guo et al., 2018; Jin et al., 2006; Jung et al., 2016; Wilson et al., 2018; Yang et al., 2002). However, it also indicates a potential for developing proxies of sediment grain-size based on measurements of elemental geochemistry. In recent decades, XRF scanning technology has enabled rapid, non-destructive, and near-continuous measurements to be made of many chemical elements in sediment cores, not only in the laboratory but also on board ships and in the field (Jansen et al., 1998; Richter et al., 2006; Ziegler et al., 2008). Although results from XRF core scanning ('element counts') are semi-quantitative (Weltje and Tjallingii, 2008; Lyle et al., 2012;

Weltje et al., 2015; Chen et al., 2016), the technique has been successfully applied to provide high-resolution geological tracers for multiple sediment components and processes, including siliceous (Jaccard et al., 2010; Jaccard et al., 2013; Wu et al., 2017) and calcareous productivity (Jaccard et al., 2010; Lyle and Backman, 2013), marine organic carbon content (Ziegler et al., 2008), and silicate rock weathering intensity (Tian et al., 2011). In light of the 'grain-size effect', this technique also holds the potential to provide useful information on sediment grain-size composition (Liu et al., 2019).

Two elements that are known to carry sediment grain-size information are zirconium (Zr) and rubidium (Rb) (Dypvik and Harris, 2001). Zirconium is mainly enriched in heavy mineral species, particularly zircon ($ZrSiO_4$), which is formed by various magmatic and metamorphic processes (Fralick and Kronberg, 1997). Zircon is widely distributed in natural sediments and usually has a relatively coarse grain-size, because it is hard, stable, and resistant to physical and chemical weathering (Pettijohn, 1941). In contrast, Rb is a typical dispersed element species, and with no Rb-dominated minerals in the natural environment (Fralick and Kronberg, 1997; Taylor, 1965), it is found mainly in K-rich minerals, such as mica, illite, and K-feldspar (Dypvik and Harris, 2001). Both Zr-rich and Rb-bearing minerals are transported and sorted together with other mineral grains, and consequently the Zr/Rb ratio in sediments can potentially be related to grain-size variations (Dypvik and Harris, 2001).

The zirconium/rubidium (Zr/Rb) ratio has been widely used in studies on loess-paleosol sequences, where it indicates mean depositional grain-size variations with no influence from pedogenesis or post-depositional weathering, thereby providing a proxy for the East Asian winter monsoon strength (Chen et al., 2006; Liu et al., 2004). However, the association between sedimentary Zr/Rb ratio and grain-size is not yet well established in marine sediments, especially in glaciomarine sediments from the Southern Ocean, where sedimentation is influenced by multiple provenance sources and transport processes including wind, ocean currents, sea ice, and icebergs (Lamy et al.,

2015; Lamy et al., 2014; McCave et al., 2014; Weber et al., 2014; Weber et al., 2012). In a few recent studies, the Zr/Rb ratio has been used as a proxy for past changes in grain-size, and hence bottom current speeds, in the vicinity of the Drake Passage (Lamy et al., 2015; Toyos et al., 2020). With the Southern Ocean increasingly viewed as a key area for understanding past and future global climate evolution (e.g. DeConto and Pollard, 2016; Jaccard et al., 2016; Schloesser et al., 2019; Sigman et al., 2010; Wilson et al., 2020), the development of new and convenient sedimentary proxies that can be applied in this region is an important target (e.g. Wu et al., 2019).

In this study, we report high-resolution Zr/Rb ratios, measured by both ICP-MS and XRF scanning techniques, and conventional grain-size data from a series of sediment cores collected from the Prydz Bay and Ross Sea regions of the Southern Ocean. In combination with published data from cores in the Drake Passage, we evaluate the potential of the Zr/Rb count ratio from XRF scanning as a proxy for grain-size variations in glaciomarine sediments. This study is arranged as follows. First, since previous studies on sedimentary Zr/Rb ratios were mainly based on quantitative geochemical analyses (e.g. Chen et al., 2006; Liu et al., 2004), the robustness of Zr/Rb count ratio data from XRF scanning is tested by comparison to concentration data measured by ICP-MS. Second, the grain-size information carried in the Zr/Rb count ratio is identified by comparison to the measured grain-size spectra, with support from the results of grain-size separation experiments. Finally, the strengths and potential limitations of using the XRF scanning derived Zr/Rb count ratio as a proxy for sediment grain-size variations are discussed.

2 Environmental setting of the Southern Ocean

The Southern Ocean is the water territory surrounding Antarctica, and its ocean currents transport heat, salt, and nutrients between the Pacific, Atlantic, and Indian Oceans (Bostock et al., 2013; Rintoul et al., 2010). It is also influenced by the major upwelling branch of the Meridional Overturning

Circulation (Marshall and Speer, 2012) and is recognised as a key region for atmospheric and oceanic CO_2 exchange (Anderson et al., 2009; Jaccard et al., 2013; Jaccard et al., 2016; Marshall and Speer, 2012; Sigman et al., 2010).

The surface of the Southern Ocean contains a series of oceanic fronts, defined by gradients in water properties including temperature, salinity, and nutrient concentrations (Orsi and Whitworth, 2005; Orsi et al., 1995; Fig. 1A). From south to north, they are the Southern Antarctic Circumpolar Current Front (SACCF), Polar Front (PF), Subantarctic Front (SAF), and Subtropical Front (STF) (Orsi et al., 1995). These fronts divide the surface of the Southern Ocean into several zones, including the Antarctic Zone (AZ) south of the PF, the Polar Frontal Zone (PFZ) between the PF and SAF, and the Subantarctic Zone (SAZ) between the SAF and STF.

There are two major branches of oceanic currents in the Southern Ocean, namely the Antarctic Circumpolar Current (ACC) and the Antarctic Slope Current (ASC) (Orsi et al., 1995). The ACC reaches from the surface to the seafloor and flows eastwards, driven by the Southern Westerly Winds and bounded by the SACCF and the STF (Orsi et al., 1995). The ASC is driven by the Southern Easterly Winds and flows westwards over the Antarctic continental shelf and slope (Mathiot et al., 2011). Between the ACC and ASC is the cyclonic Antarctic Divergence Zone (ADZ), which is represented by a series of mesoscale eddies forming under the shear stress of the Southern Westerly Winds and the Southern Easterly Winds (Meijers et al., 2010). The ADZ can intrude onto the Antarctic continental shelf, thereby supplying relatively warm and salty Circumpolar Deep Water (Yabuki et al., 2006). Additionally, over broad Antarctic continental shelf regions such as those of the Weddell Sea, Ross Sea, and Prydz Bay, cyclonic gyres dominate the oceanic transport.

Because of the cold climate conditions, the Southern Ocean is influenced by the presence of sea ice and icebergs. Satellite observations show that the maximum sea ice cover occurs in austral winter, with an area of ca. 18.3×10^6

180 km^2 during September forming a continuous ring around Antarctica, while
181 minimum sea ice cover occurs in austral summer, with an area of ca. 3×10^6
182 km^2 in February (Comiso, 2010). Icebergs in the Southern Ocean are mainly
183 distributed along the pathway of the ASC and in gyres over the Antarctic
184 continental shelf and slope, but they can also be transported further
185 northwards (Budge and Long, 2018), leading to the discharge of Iceberg
186 Rafted Debris (IRD) across the entire Southern Ocean.
187
188 **3 Materials**
189 Materials used in this study were obtained from four sediment gravity cores
190 ANT30/P1-02 (P1-2), ANT30/P1-03 (P1-3), ANT29/P4-01 (P4-1), and
191 ANT31/JB06 (JB06) retrieved during the 29th, 30th, and 31st Chinese Antarctic
192 Research Expeditions onboard *R/V Xuelong* in 2012-2013, 2013-2014 and
193 2014-2015, respectively (Fig. 1, Table 1). Our major focus is on cores P1-2 and
194 JB06.
195 Cores P1-2 (624 cm in length), P1-3 (599 cm), and P4-1 (421 cm) were
196 retrieved from the lower continental slope and continental rise near Prydz Bay,
197 East Antarctica in water depths of 2542-3162 m (Fig. 1B, Table 1). The colour
198 of these cores varies cyclically between olive, brown, and grey. The core
199 sediment principally consists of structureless clayey silt and silty clay, with a
200 minor proportion of sand (63-2000 μm) and a few randomly distributed
201 dropstones (> 2 mm). Age models for these cores were established previously
202 (Wu et al., 2017) by tuning their export production records to the LR04 benthic
203 $\delta^{18}O$ stack (Lisiecki and Raymo, 2005), because extremely poor carbonate
204 preservation prevents the application of oxygen isotope stratigraphy.
205 Core JB06 (299 cm in length) was collected from the JOIDES Trough on
206 the western outer continental shelf of Ross Sea, East Antarctica in a water
207 depth of 568 m (Fig. 1C, Table 1). The colour of the core changes from light
208 and dark grey at the bottom to olive at the top. The core sediments are coarser
209 than in core P1-2 and are mainly composed of clayey silt and sandy clayey silt.

Sand (>63 μm) fractions mostly occur in the core depth interval from 70-230 cm, with a few randomly distributed dropstoones. Carbonates are rare in the core sediments, except towards the bottom between 240-270 cm core depth, where benthic foraminifera *Cassidulina sp.* are abundant. No age model has been established for this core yet. However, previous studies from the Ross Sea indicate that such benthic foraminifera-rich sediments were deposited in a sub-ice shelf environment during the last glacial period (< 36 ka ^{14}C age, Taviani et al., 1993; Yokoyama et al., 2016).

In addition to these four cores, we also refer to two other cores from previous studies in the vicinity of the Drake Passage (Fig. 1, Table 1).

4 Methods

Experimental methods used in this study include geochemical analyses by XRF core scanning and ICP-MS, grain-size measurements, and water content measurements. All measurements on core JB06 are reported here for the first time. Grain-size measurements on core P1-2 (Wu et al., 2018) and XRF core scanning on cores P1-2, P1-3, and P4-1 (Wu et al., 2017) have been conducted previously, but Zr and Rb counts of these cores are reported and discussed here for the first time. Down core ICP-MS measurements were only conducted on core P1-2. Water content was measured only on core JB06. We also conducted Rb and Zr concentration measurements by ICP-MS on separated grain-size fractions from cores P1-2 and JB06 (see Section 4.3). All measurements were carried out at the State Key Laboratory of Marine Geology, Tongji University, Shanghai, China, except for the grain-size separation experiment, which was carried out at Qingdao Sparta Analysis & Test Co. Ltd., Qingdao, China.

4.1 XRF core scanning

XRF core scanning measurements were obtained directly on the split core surface of the archive half of each core using an AVAATECH XRF core

scanner at 1 cm intervals. The split core surface was covered with a spex certiprep 3532 Ultralens foil (4 μm thick) to protect the probe of the scanner from contamination and to prevent desiccation of the sediment. A Pd filter was placed in front of the incoming X-ray beam and measurements were taken at 1 cm resolution with a size of 1 cm × 1 cm. Each core was triple-scanned for elements from Al to Ba at 1 mA at different tube voltages (10 kV, 30 kV, 50 kV) with 30 s counting time. Further technical details relating to the XRF core scanner are described in Richter et al. (2006).

4.2 ICP-MS

For quantitative Rb and Zr analyses on core P1-2, dry bulk sediment was sampled at 2 cm intervals, finely ground and ashed at 600 °C for 2 h to measure the loss on ignition, and digested in a concentrated $HF+HNO_3$ mixture, together with a series of Chinese and USGS rock and sediment reference materials, before analysis by ICP-MS (IRIS advantage) (Wei et al., 2003). The relative standard deviation (RSD), as calculated from the reference materials, is generally better than 5 % for Rb and Zr. Duplicate measurements on randomly selected samples also indicate a very good reproducibility (RSD <5 %).

4.3 Grain-size separation experiment

To evaluate the relationship between grain-size and Zr and Rb concentrations, we conducted a grain-size separation experiment. Previous such experiments on loess have typically divided the sediment into <2 μm, 2-8 μm, 8-20 μm, 20-32 μm, and >32 μm fractions, because loess is mainly composed of clay- and silt-sized sediment (e.g. Chen et al., 2006; Liu et al., 2002). Because our samples contain significant proportions of sand, we followed the above divisions, but further divided the >32 μm fraction into 32-63 μm, 63-150 μm, 150-250 μm, and >250 μm fractions. Briefly, a sample from each of cores P1-2 and JB06 was leached with 30 % H_2O_2 and 1 mol/L acetic

acid to remove organic matter and carbonate, respectively. The residues were then separated based on Stokes' settling velocity law into <2 μm, 2-8 μm, 8-32 μm, and >32 μm fractions using a centrifuge, according to Chen et al. (2006). The >32 μm fractions were further separated into 32-63 μm, 63-150 μm, 150-250 μm and >250 μm fractions by sieving. The separated fractions were digested and measured by ICP-MS for Rb and Zr concentrations, following the procedures described in Section 4.2.

4.4 Sediment grain-size

Grain-size measurements were conducted at 2 cm intervals. For this analysis, 0.15 g of dry bulk sediment from each sample was successively treated with 10 % H_2O_2, 1.0 N HCl, and 2.0 N NaOH in a water bath at 85 °C to remove organic carbon, carbonate, and biogenic silica. After confirming the successful removal of all biogenic components by microscope inspection, the samples were soaked in 20 mL distilled water and dispersed by an ultrasonicator for 2 min, followed by analysis using an Automatic Laser Analyzer (Beckman Coulter LS230) (Wu et al., 2018). Such a particle size analyser can be used for grain-size analysis in the range of 0.375-2000 μm. The analytical reproducibility was assessed using the Normalised Euclidian Distance (ND), according to Jonkers et al. (2015). Measurements on 10 randomly-selected duplicate samples indicate NDs that are all less than 0.02 (2 %), indicating good reproducibility.

To investigate if the core sediments were subject to significant bottom current sorting, sortable silt mean grain-size (SSM) and sortable silt percent (SS%, defined as the 10-63 μm fraction relative to the <63 μm fraction) were calculated after McCave et al. (1995). These parameters have previously been calculated for core P1-2 (McCave and Andrews, 2019).

It should be noted that our grain-size data was measured by laser particle sizer. Previously, McCave et al. (2006) criticised this approach for the determination of fine particle sizes on the grounds that shape effects could

lead to slow-sinking platy particles below 10 μm in diameter leaking into the > 10 μm range. However, such shape effects appear to be insignificant for glacial sediments from high latitude oceans (Konert and Vandenberghe, 1997), which has been confirmed by recent studies using laser sizer derived grain-size (Li and Piper, 2015; Mao et al., 2018; Marshall et al., 2014; McCave and Andrews, 2019).

To further explore the association between the Zr/Rb geochemistry and grain-size composition, we also defined a new variable, partial mean grain-size (PMG), which is defined as the mean grain-size of the interval from the finest grain-size bin (0.375 μm) to a coarser grain-size bin, as follows:

$$PMG_{g_m} = \frac{\sum_{i}^{m} g_i f_i}{\sum_{i}^{m} f_i} \quad \text{Eq. (1)}$$

where m is the serial number of a specified grain-size (μm); g_i and f_i represent the grain-size of the i-th grain-size bin and the volume percent of the i-th grain-size bin, respectively; and PMG_{g_m} means the PMG of the $< g_m$ μm fractions. For instance, PMG_{63} represents the partial mean grain-size of the <63 μm fraction (m=56, g_{56}=63).

4.5 Water content

Water content was measured at 2 cm intervals in core JB06. 25-35 g freshly split samples were weighed, then dried at 55 °C for 72 h and re-weighed. Water content was calculated as follows (Wu et al., 2019):

$$WatCon = \frac{(Mw - Md)}{Mw} \times 100\% \quad \text{Eq. (2)}$$

where *WatCon* represent water content (wt.%), and *Mw* and *Md* refer to the weights of wet and dried samples, respectively.

5 Results

5.1 Core ANT30/P1-02

Downcore distributions of Rb and Zr in core P1-2 from both XRF core scanning and ICP-MS measurements show consistent glacial-interglacial variations (Fig. 2A-B). In the Rb records, higher/lower values mainly coincide with cold/warm periods respectively, except during glacial marine isotope stage (MIS) 12, in which the values are as low as during the subsequent interglacial MIS 11. In contrast, the Zr records usually show higher values during interglacial periods and lower values during glacial periods. In the Zr/Rb ratio records (Fig. 2C), the glacial-interglacial variation is even clearer than in the Rb and Zr records, with higher values during interglacial periods and lower values during glacial periods (including glacial MIS 12). The XRF scanning derived and ICP-MS derived Zr/Rb records display better consistency than the individual Rb and Zr records.

The grain-size of the core sediment is dominated by the 1-10 μm fraction (Fig. 2F), with the exception of two intervals with high sand content at ~365 ka and ~465 ka. Changes in mean grain-size exhibit a similar pattern to the Zr/Rb ratio (Fig. 2C cf. Fig. 2D). Despite the visual similarity, the correlation coefficient between the two records is only 0.07 (N=309). However, after removing the extreme samples with high sand content (coloured red in Fig. 2D), the correlation between the Zr/Rb ratio and the mean grain-size records improves significantly to 0.55 (N=300).

The SSM varies between 14 μm and 25 μm, with an average of 20 μm, and the SS% varies between 8 % and 49 %, with an average of 25 % (Fig. 2E). The SSM and SS% show significant glacial-interglacial fluctuations, but the temporal patterns of the two records differ during some intervals. Interestingly, the SSM record shows a temporal pattern rather similar to the mean grain-size record (Fig. 2D), while the temporal pattern of the SS% is more similar to changes in the Zr/Rb ratio (Fig. 2C).

5. 2 Core ANT31/JB06

In core JB06, the water content ranges from 20-80 wt.% (Fig. 3A). It varies

irregularly between 20-50 wt.% around an average value of ~30 wt.% in the lower 150 cm of the core, and then increases irregularly towards the core top.

Rubidium (Fig. 3B) and Zr (Fig. 3C) counts show co-varying downcore changes in the upper 210 cm, whereas an inverse pattern emerges in the lower part of the core. The downcore pattern of the Zr/Rb count ratio (Fig. 3D) mostly follows that of the Zr count, with significant variability in the lower ~90 cm and a decreasing trend towards the core top. Generally, these records exhibit significant negative correlations with the water content (Fig. 3A), with correlation coefficients between the water content and Rb and Zr counts of -0.81 and -0.78 (N=148), respectively. The correlation coefficient between the water content and the Zr/Rb count ratio is much lower, at -0.44 (N=148).

The core sediment is characterised by a higher fine sand content in the lower ~160 cm and a higher silt fraction in the upper ~140 cm (Fig. 3G). The mean grain size varies between 11-104 μm (Fig. 3E), with an average of 39 μm and a generally decreasing trend towards the core top. Intervals with higher mean grain-size values correspond to intervals with higher fine sand content. The mean grain-size is positively correlated with the Zr/Rb count ratio, but the correlation coefficient is only 0.34 (N=148).

The SSM varies between 19 μm and 40 μm, with an average of 26 μm, and the SS% varies between 32 % and 88 %, with an average of 53 % (Fig. 3F). Downcore patterns of the two records are rather consistent, and both are similar to the Zr/Rb count ratio (Fig. 3D), with the closest match arising for the SS% record (e.g. compare records at ~290 cm).

5.3 Regional comparison of Zr/Rb in Prydz Bay sediment cores

Temporal patterns of the XRF scanning derived Rb, Zr, and Zr/Rb ratios in cores P1-3 and P4-1 are consistent with those of core P1-2. Hence, both the pattern and amplitude of glacial-interglacial variations appear to be reproducible across multiple cores in Prydz Bay (Fig. 4).

5.4 Grain-size separation experiment

The distributions of Rb, Zr, and Zr/Rb against grain-size are fairly consistent between the two cores (Fig. 5). Rubidium concentration varies between 100-240 ppm in core P1-2 and between 45-180 ppm in core JB06, being higher in core P1-2 than core JB06 for all grain-size classes (Fig. 5A). In core JB06, Rb decreases with increasing grain-size across the whole grain-size spectrum, while in core P1-2 Rb decreases with increasing grain-size in the <63 μm fraction but then slightly increases with increasing grain-size in the >63 μm fraction. In contrast, Zr concentrations are comparable in the two cores, varying between 104-327 ppm in core P1-2 and between 77-254 ppm in core JB06 (Fig. 5B). In both cores, Zr content increases with increasing grain-size in the <63 μm fraction and decreases significantly with increasing grain-size in the >63 μm fraction. The Zr/Rb ratio varies between 0.5-3.0 in core P1-2 and 0.8-3.1 in core JB06 (Fig. 5C), with slightly higher values in core JB06 than in core P1-2 for all grain-size classes. We also note that the distribution of Zr/Rb approximately follows the Zr concentration: it increases with increasing grain-size in the <63 μm fraction and decreases with increasing grain-size in the >63 μm fraction.

6 Discussion

6.1 Relationship between Zr/Rb ratios from ICP-MS and XRF scanning

XRF scanning data are widely regarded as semi-quantitative due to specimen and matrix effects. The specimen effect relates to the inhomogeneity and irregular measurement geometry of the specimen (Jenkins, 2012; Vries and Vrebos, 2002), which can be reduced by smoothing the split core surface to be scanned (Richter et al., 2006), while the matrix effect describes the influence of inter-element interactions. The matrix effect is a non-linear function of the concentrations of all the elements present, which can induce scattering, absorption, and enhancement effects on the intensities of the element of interest (Weltje et al., 2015; Weltje and Tjallingii, 2008). In particular,

variability in water content linked to changes in the sedimentary phases present and/or the extent of compaction usually imparts a significant matrix effect (Chen et al., 2016; Lyle and Backman, 2013; Tjallingii et al., 2007).

In our records, the minor discrepancies between Rb and Zr derived from XRF scanning and ICP-MS measurements in core P1-2 could be interpreted as a result of matrix and/or specimen effects (Figs. 2A and 2B), while the Rb and Zr counts in core JB06 are clearly affected by changes in water content (Figs. 3A-C). Hence, the relationship between Zr and Rb data derived from XRF scanning and ICP-MS measurement needs to be carefully explored.

In order to convert element counts from XRF scanning into element concentrations, early studies usually applied the general linear regression technique (e.g. Jansen et al., 1998; Tjallingii et al., 2007). However, these studies did not consider the matrix and specimen effects (Weltje and Tjallingii, 2008), which can lead to considerable scatter and bias in cross-plots of intensity versus concentration, as evidenced in our Rb and Zr data (Figs. 6A and 6B). More recently, studies have highlighted that corrections for interstitial water content can improve the conversion of counts to concentration (Lyle et al., 2012; Chen et al. 2016). However, these studies focused mainly on long-term trends of element distributions, and were able to reduce but not eliminate matrix effects (Lyle et al., 2013; Chen et al. 2016).

In parallel, based on the theory of XRF spectroscopy and principles of compositional data analysis, Weltje and Tjallingii (2008) proposed a log-ratio calibration equation (LRCE) for relating element count ratios from XRF scanning to element concentration ratios, as follows:

$$\ln\left(\frac{W_{ij}}{W_{iD}}\right) = \alpha_{jD}\ln\left(\frac{I_{ij}}{I_{iD}}\right) + \beta_{jD} \qquad \text{Eq. (3)}$$

where W_{ij} and W_{iD} represent the concentrations (weight proportion) of elements j and D in specimen i; I_{ij} and I_{iD} represent the net intensity of elements j and D in specimen i from XRF scanning; and the coefficients α_{jD} and β_{jD} represent the matrix effect and machine detection efficiency,

446 respectively, for element j relative to element D. The LRCE has been further
447 updated to a multivariate calibration equation that better accounts for the
448 matrix effect and is able to predict bulk element concentrations (Weltje et al.,
449 2015), but here we are interested in only the Zr/Rb ratio and hence consider
450 Eq. (3) to be sufficient.

451 For a specific elemental ratio, the specimen effect is eliminated and α_{jD} and
452 β_{jD} in Eq. (3) become constants, because two simultaneously measured
453 elements are subject to the same specimen effect and a covariant matrix effect
454 (Weltje and Tjallingii, 2008). Since both Zr and Rb counts were measured at 30
455 kV voltage, Eq. (3) is appropriate for describing the relationship between the
456 Zr/Rb count ratio and concentration ratio, as follows:

457 $$\ln\left(\frac{W_{iZr}}{W_{iRb}}\right) = \alpha_{Zr-Rb}\ln\left(\frac{I_{iZr}}{I_{iRb}}\right) + \beta_{Zr-Rb} \qquad \text{Eq. (4)}$$

458 where W_{iZr} and W_{iRb} represent the concentrations of Zr and Rb in specimen *i*;
459 I_{iZr} and I_{iRb} represent the net intensity of Zr and Rb in specimen *i* from XRF
460 scanning; and the coefficients $\alpha_{Zr\text{-}Rb}$ and $\beta_{Zr\text{-}Rb}$ represent the matrix effect and
461 machine detection efficiency, respectively, for Zr relative to Rb.

462 Eq. (4) indicates that the Zr/Rb count ratio should be linearly correlated
463 with its concentration counterpart on a log-log plot. Indeed, our ln(Zr/Rb)
464 concentration data from ICP-MS and ln(Zr/Rb) count ratio from XRF scanning
465 are in good agreement with this relationship (r = 0.83, N = 309. Fig. 6C). In
466 practice, the Zr/Rb concentration ratio in a given sediment core is expected to
467 vary over a limited range, leading to strong correlations between the Zr/Rb
468 ratio and its logarithm, namely:

469 $$\ln\left(\frac{W_{iZr}}{W_{iRb}}\right) = c_1\frac{W_{iZr}}{W_{iRb}} + c_2 \qquad \text{Eq. (5)}$$

470 where c_1 and c_2 are constants that represent the slope and intercept,
471 respectively, of the linear relationship. In core P1-2, the Zr/Rb concentration
472 ratio varies between 0.6 and 1.4, and the correlation coefficient between the
473 Zr/Rb concentration ratio and its logarithm is 0.999 (N=312, Fig. 6D).

Consequently, ln(Zr/Rb) count ratios from XRF scanning can be calibrated to derive Zr/Rb concentration ratios (r = 0.88, N = 309; Fig. 6E), according to:

$$\frac{W_{iZr}}{W_{iRb}} = \alpha \ln\left(\frac{I_{iZr}}{I_{iRb}}\right) + \beta \qquad \text{Eq. (6)}$$

where

$$\alpha = \frac{\alpha_{Zr-Rb}}{c_1} \qquad \text{Eq. (7)}$$

$$\beta = \frac{\beta_{Zr-Rb} - c_2}{c_1} \qquad \text{Eq. (8)}$$

To test the robustness of the calibration, we applied a non-parametric bootstrap re-sampling algorithm to the Zr/Rb dataset of core P1-2. Ten thousands replicates were generated using a uniform distribution pseudo-random number generator, with a sample size for each replicate of 18, which is the square root of the total number of samples (309) (Efron and Tibshirani, 1994). The result shows that both α and β parameters obey normal distributions (Figs. 7A-B). Furthermore, applying this calibration to the downcore ln(Zr/Rb) count data from XRF scanning produces estimates of Zr/Rb concentration ratios that closely match the measured ICP-MS data (Fig. 7C). Together, these observations support the robustness of the linear relationship between the ln(Zr/Rb) count ratio and the Zr/Rb concentration ratio. In addition, the consistent temporal variations of the ln(Zr/Rb) count ratio recorded in three Prydz Bay cores (i.e. P1-2, P1-3, and P4-1; Fig. 4) supports the general reliability of the ln(Zr/Rb) ratio as a proxy for regional paleoenvironmental change, because these cores were retrieved from the same sedimentary environment and are expected to record a similar pattern of past changes (Wu et al., 2017, 2019).

6.2 Relationship between Zr/Rb ratio and grain-size of Southern Ocean sediments

In continental loess-paleosol sequences, significant correlations exist between the Zr/Rb concentration ratio and the mean grain-size in the loess intervals, whereas the correlations are poor in the paleosol intervals (Chen et al., 2006; Liu et al., 2002; Liu et al., 2004). The relationship breaks down in the paleosols because pedogenesis under warm humid conditions modifies the grain-size distribution of the deposits, while the Zr/Rb ratio remains unchanged (Chen et al., 2006; Liu et al., 2002; Liu et al., 2004). Our records also demonstrate clear links between grain-size parameters and Zr/Rb ratios (Fig. 2, 3), but there are some discrepancies between the Zr/Rb ratio and the mean grain-size of the bulk sediment (e.g. Fig. 2D cf. Fig. 2C). Unlike in paleosol sequences, these differences cannot be attributed to post-depositional modifications, because such processes are largely restricted by the low temperatures of the Southern Ocean (Ehrmann et al., 1992) and low dissolved oxygen availability on the seafloor (Garcia et al., 2009). Hence, the relationship between the Zr/Rb ratio and the grain-size of Southern Ocean sediments requires careful consideration.

6.2.1 Relationship between ln(Zr/Rb) and grain-size distributions

Grain-size separation experiments on loess show that, with increasing grain size, decreases in Rb concentration and increases in Zr concentration are monotonous (Chen et al., 2006; Liu et al., 2002). In our samples, such a relationship appears to hold only in the <63 μm fraction (Fig. 5), especially for Zr which peaks in the 32-63 μm fraction and then decreases significantly with increasing grain-size in the sand fraction (Fig. 5B). The enrichment of Rb in the fine sediments (Fig. 5A) is consistent with its predominant association with clay minerals, although the presence of minor Rb in the coarser fractions may indicate its additional occurrence in K-feldspar or mica. For Zr, its enrichment within a limited grain-size range (i.e. ~8-150 μm; Fig. 5B) may indicate that zircon, as the likely major host mineral, is predominantly present in this grain-size range.

Overall, the grain-size separation experiment confirms the grain-size-dependence of the Zr/Rb ratio in marine sediments (Fig. 5C), but only provides relatively low grain-size resolution. To explore the association between grain-size and Zr/Rb geochemistry in more detail for each of the studied cores, we calculated spectra of the correlation coefficient between the downcore XRF scanning derived ln(Zr/Rb) count ratio and both the volume percent of each grain-size bin (Fig. 8A-B) and the partial mean grain-size (Fig. 8C-D).

In core P1-2 (Fig. 8A), the ln(Zr/Rb) ratio is negatively correlated with the <6 μm fractions, which include clay and fine silt, and is positively correlated with the 7-63 μm fractions, which represent medium and coarse silt. At larger grain-sizes, the correlation with the sand (>63 μm) fractions is generally statistically insignificant (p >0.01). The 4-10 μm interval represents a transition from negative to positive correlations, while the 50-90 μm interval is a region where the positive correlation rapidly becomes poor.

In core JB06, the correlation spectrum shows a similar pattern to core P1-2, but with different threshold values (Fig. 8B cf. Fig. 8A). In this core, the ln(Zr/Rb) ratio is negatively correlated with the <23 μm fractions, which include clay and fine to medium silt, and is positively correlated with the 30-100 μm fractions, which include medium to coarse silt and fine sand. Its correlation with coarser sand fractions is negative or insignificant. There are also two major transitions in the correlation coefficient, but at different grain-size intervals than in core P1-2. The first transition is from negative to positive correlations over the 20-40 μm interval, while the second transition is over the 90-120 μm interval, where the correlation rapidly becomes poor and/or insignificant.

Overall, the correlation spectra are consistent with the distribution of the Zr/Rb concentration ratio in our grain-size separation experiment (Fig. 5C), but provide much higher grain-size resolution. In the two transition zones (Fig. 8A-B), the correlation relationship between the ln(Zr/Rb) ratio and grain-size changes dramatically. The first transition zone represents changes from

Rb-dominated to Zr-dominated sediment fractions (Fig. 5) and is located close to 10 μm, which represents the approximate boundary between cohesive (<10 μm) and non-cohesive (>10 μm) sediment fractions (McCave et al., 1995). The second transition zone occurs around the grain-size of fine sand, and corresponds to significant decreases in Zr concentrations and Zr/Rb concentration ratios (Fig. 5). Comparing the spectra of correlation with the average grain-size distributions (Fig. 8A-B, shaded areas), it is clear that the majority of the sediment in these cores comprises grain-size fractions finer than those of the second transition zone (i.e. approximately the <63 μm fraction in core P1-2 and the <100 μm fraction in core JB06).

In the spectra of correlation coefficients between the ln(Zr/Rb) and the partial mean grain-size (Fig. 8C-D), high positive correlation coefficients are present between the ln(Zr/Rb) ratio and PMG_{63} in core P1-2, and between the ln(Zr/Rb) ratio and PMG_{100} in core JB06. The correlation then decreases rapidly with the progressive inclusion of >63 μm fractions in core P1-2 and >100 μm fractions in core JB06.

In summary, these analyses indicate that the ln(Zr/Rb) ratio mainly reflects the grain-size composition of the relatively fine fractions which comprise the majority of the core sediments, with only a minor influence from the relatively coarse fractions (i.e. >63 μm fraction in core P1-2, and >100 μm fraction in core JB06).

6.2.2 Limited influence of coarse IRD fractions on ln(Zr/Rb) ratios

In the open Southern Ocean, coarse sediment fractions >63 μm or >100 μm are often considered to be predominantly derived from iceberg rafted debris (IRD), because bottom currents are typically too weak to move and sort lithic grains of such a diameter (Lamy et al., 2015; McCave and Andrews, 2019). Scatter plots between the coarse fraction percent and the bulk mean grain-size show significant positive correlations (Figs. 9A and 9D), indicating that the addition of IRD to the sediment biases the mean grain-size towards

coarser values (Jonkers et al., 2015) (see also Figs. 2 and 3). In contrast, the lack of correlation between the coarse fraction percent and the ln(Zr/Rb) ratio (Figs. 9B and 9E) suggests that IRD input does not significantly perturb the ln(Zr/Rb) ratio of the bulk sediment.

Coarse IRD in the Southern Ocean is predominantly composed of quartz (e.g. Teitler et al., 2010; Williams et al., 2010) because it is abundant in Antarctic source rocks and resistant to weathering. For both studied cores, sieving and microscope inspection indicate that the >63 μm fraction is predominantly composed of quartz (>85 %), with minor rock and other mineral fragments (<10 %), and biogenic fragments (e.g. foraminifera, radiolarians, and sponge spicules; 0-15 %). Neither quartz nor biogenic fragments are expected to be rich in Rb or Zr, which is consistent with the low Rb and Zr concentrations in the separated >63 μm fractions (Figs. 5A-B). In addition, the coarse IRD fractions account for only modest proportions of the total sediment (<50%, usually <25 %, with an average of ~10 %, see Fig. 9). Together, these factors explain the lack of influence of the coarse IRD fraction on the ln(Zr/Rb) ratios, and hence the potential for IRD inputs to decouple ln(Zr/Rb) ratios from the bulk sediment mean grain-size (e.g. Figs. 2, 3).

6.2.3 Role of local hydrodynamics

The sensitivity of the Zr/Rb ratio to grain-size diminishes, and is ultimately lost, in the >63 μm fraction in core P1-2 and in the >100 μm fraction in core JB06 (Fig. 8). Here we suggest that the different grain-size value characterising this second transition zone in the two cores is mainly determined by local hydrodynamics.

In core JB06, there is no correlation between the > 100 μm fraction and the SSM (Fig. 9F), while downcore variations of the SSM and SS% (Fig. 3F) are characterised by a correlation coefficient of 0.86 indicating that the sediment is current-sorted (McCave and Andrews, 2019). In the modern ocean, bottom current speeds in the Western Ross Sea range from tens of cm/s to >1 m/s,

620 primarily composed of a tidal (barotropic) component and a benthic gravity
621 component (Gordon et al., 2004). The SSM values of core JB06 increase
622 towards the base of the core (Fig. 3F), indicating that the vigour of the local
623 bottom current was even stronger in the past than today. Such a strong local
624 bottom current is comparable to or stronger than those inferred from sediment
625 cores in the Drake Passage region (Lamy et al., 2015; Toyos et al., 2020), and
626 hence would be sufficient to sort fine sand as well as silt fractions (Lamy et al.,
627 2015; Mao et al., 2018; McCave and Andrews, 2019).

628 In contrast, in core P1-2, the SSM and SS% have different temporal
629 patterns (Fig. 2E) and a correlation coefficient of only 0.37 (N=312), which
630 implies that the bulk sediment generally lacks significant features of bottom
631 current sorting. Since the SSM and the sand percent (>63 μm) show a
632 correlation (Fig. 9C), the SSM was potentially affected by the input of IRD.
633 Nevertheless, the much finer SSM values in core P1-2 than in core JB06 would
634 tend to suggest slower flow speeds, consistent with a modern bottom current
635 speed near the core site of <5 cm/s (Meijers et al., 2010). The average and the
636 highest SSM values in the record are 20 μm and 25 μm, which are 2 μm and 7
637 μm higher than the core top value (18 μm). If those values are taken at face
638 value, applying a modern current speed of 5 cm/s (Meijers et al., 2010) and the
639 universal flow speed versus grain-size calibration gradient (McCave et al.,
640 2017), we estimate that the local bottom current has averaged ~8 cm/s and
641 has not been above ~15 cm/s over the last 523 kyr. These speeds are much
642 slower than at site JB06, and hence would be unable to impart a
643 current-sorting signature on the fine sand fraction (e.g. Jonkers et al., 2015).

644 In summary, when bottom currents are very strong, they can sort fine sand
645 fractions in addition to silt, and in such a case the fine sand fractions derived
646 from IRD would also be sorted. This scenario would enable sorting of Zr- and
647 Rb-bearing minerals within these fractions, thereby generating significant
648 correlations between the Zr/Rb geochemistry and the content of these
649 grain-size fractions. Indeed, our Zr/Rb and grain-size data from the Ross Sea

core JB06 (Figs. 8B, 8D) may be taken as a confirmation that fine sand fractions in this region can be transported by ocean currents. This observation reiterates the importance of using a coarser grain-size diameter (e.g. >150 μm or 250 μm) to define IRD in the Southern Ocean (e.g. Passchier, 2011; Wilson et al., 2018).

6.2.4 Relationship between grain-size parameters and ln(Zr/Rb) in the Southern Ocean

Based on the correlation analysis between ln(Zr/Rb) and grain-size (Fig. 8), a series of grain-size parameters would be expected to be related to downcore changes in ln(Zr/Rb). For core P1-2, we plot the partial mean grain-size of the <63 μm fraction (PMG_{63}) (Fig. 10A), the ratio of the volume percent in the 7-63 μm and the <6 μm fractions (Fig. 10B), the SS% (Fig. 10C), and the SSM (Fig. 10D). For core JB06, we plot the partial mean grain-size of the <100 μm (PMG_{100}) (Fig. 11A), the ratio of the volume percent in the 30-100 μm and the <23 μm fractions (Fig. 11B), the SS% (Fig. 11C), and the SSM (Fig. 11D). Although not perfect, the parameters PMG_{63} of core P1-2 and PMG_{100} in core JB06 can be considered to provide the IRD-corrected mean grain-size (i.e. the mean grain-size of the sediment after excluding unsorted coarse fractions). Together, the ln(Zr/Rb) thus mainly reflect the grain-size composition of the IRD corrected fractions of the sediments.

For both our studied cores, the SS% and ln(Zr/Rb) have consistent downcore patterns (Fig 10C cf. Fig 10E, Fig 11C cf. Fig. 11E) and are highly correlated (Fig. 12B), regardless of whether the SSM is well correlated with the SS% (JB06) or not correlated (P1-2) (Fig. 12A). The SS% and ln(Zr/Rb) show a good correlation because the major enrichments of Rb and Zr overlap with the <10 μm fraction and the 10-63 μm fraction, respectively (Figs. 5A-B, 8A-B). Therefore, if the SS% and SSM are correlated, which provides an indicator for current sorting (McCave and Andrews, 2019), the ln(Zr/Rb) and SSM will also be correlated (Fig. 12A cf. Fig 12C). Hence, in cases of current-sorting,

temporal changes in the ln(Zr/Rb) ratio will reflect relative changes of the bottom current speed. Such a scenario applies to core JB06 from the Ross Sea continental shelf, as well as to core 3128 from the southern coast of Chile (Lamy et al., 2015) and core 93-2 from the Drake Passage (Toyos et al., 2020) (Figs. 12A-C).

In cases where SSM data are available but not accompanied by SS% data, the robust relationship between ln(Zr/Rb) and SS% (Fig. 12B) could be useful in discriminating whether sediments were subject to bottom current sorting. For example, measurements by Coulter counter cannot provide information on SS%, while measuring the grain-size of fine sediment fractions (e.g. <10 μm) using a Sedigraph is highly time-consuming. In such cases, ln(Zr/Rb) ratios could provide a proxy for SS% variations.

Interestingly, although the regression lines between ln(Zr/Rb) and SS% differ between cores, their slopes are rather consistent (Fig. 12B). For the bottom current-sorted sediments (i.e. cores JB06, 3128, and 93-2), the slopes of the regression lines between ln(Zr/Rb) and SSM are also similar (Fig. 12C). These relationships are readily visualised when the core data are normalised by subtracting their respective mean values (Figs. 12D-F). Single values for the slopes may be derived by combining the datasets from multiple cores: 0.32 for SSM versus SS%, 34.1 for SS% versus ln(Zr/Rb), and 12.7 for SSM versus ln(Zr/Rb). Since these cores were retrieved from different regions of the Southern Ocean under the influence of different hydrodynamic conditions, the consistent slopes may reflect a general association between the grain-size and Zr/Rb geochemistry of glaciomarine sediments from the Southern Ocean. If validated by data from additional sediment cores, these values could provide a simple means to estimate the magnitude of changes in SS% and SSM based on the ln(Zr/Rb) ratio from XRF scanning. When combined with the universal grain-size-flow speed calibration gradient proposed by McCave et al. (2017), the magnitude of changes in flow speed could then be estimated in cases where the sediments are bottom current-sorted.

6.3 Scope for the application of ln(Zr/Rb) as a grain-size proxy

Our findings indicate that the ln(Zr/Rb) count ratio reflects IRD-corrected mean grain-size and can be used to indicate changes in bottom current strength if the sediment is current-sorted. Hence, long high-resolution records of bottom current strength can be obtained by calibrating the ln(Zr/Rb) ratios using a relatively small number of grain-size measurements on discrete samples (e.g. Toyos et al., 2020). Since the sediment core sites of our study and previous studies (Lamy et al., 2015; Toyos et al., 2020) (Table 1) are located in different regions of the Southern Ocean with different sedimentary and hydrodynamic conditions, the consistent association between ln(Zr/Rb) ratios and grain-size variations (Fig. 12) suggests a wide applicability of this approach in the Southern Ocean. In addition, the combination of these studies suggests that it can be applied over a range of temporal resolution (e.g. millennial to orbital) and time periods (e.g. tens of thousands of years to >1 Ma).

The basis for the association between ln(Zr/Rb) ratios and sediment grain-size is that the Zr/Rb geochemistry is closely related to the grain-size of lithogenic particles. Because Zr and Rb are predominantly contained in detrital minerals, the correlation between ln(Zr/Rb) and grain-size is not notably affected by processes such as biogenic deposition or authigenic mineral precipitation. In contrast, while Si/Al ratios can also be well correlated to sediment grain-size (e.g. Bouchez et al., 2011; Guo et al., 2018; Lamy et al., 2015), Si is additionally supplied to Southern Ocean sediments by the biological productivity of abundant siliceous organisms (e.g. diatoms, sponge spicules, radiolarians). If the goal is to obtain information related to current-sorting, the other major benefit of using Zr/Rb ratios is their insensitivity to the input of coarse quartz-rich IRD (Figs. 5, 9), whereas such inputs could perturb Si/Al ratios.

In a recent study, Liu et al. (2019) developed a statistical model to predict

740 sediment mean grain-size using multi-element data from XRF scanning.
741 However, when applying such a model to our downcore data (Supplement S1,
742 DR Figures 1-4), we found that only the long-term trends of the mean
743 grain-size time series can be predicted, whereas high frequency variability is
744 smoothed, particularly during intervals with abundant coarse fractions (DR
745 Figures 3, 4). Such a scenario arises in part because the geochemistry can be
746 independent of, or relatively insensitive to, the proportion and grain-size of the
747 unsorted coarse fractions (e.g. Figs. 5, 9). In addition, the elements Mn and Fe
748 are both used in that prediction model, but can be significantly affected by their
749 enrichment in oxide and oxyhydroxide phases. In the Southern Ocean,
750 Mn-oxides/hydroxides are typically authigenic in origin, and their formation
751 may be affected by changes in abyssal ventilation (e.g. Jaccard et al., 2016;
752 Jiménez-Espejo et al., 2019; Presti et al., 2011; Wu et al., 2018), while
753 Fe-oxides/hydroxides can be associated with provenance changes (e.g. Wu et
754 al., 2019). As such, these two elements may vary independent of sediment
755 grain-size in the Southern Ocean. For the above reasons, the multi-element
756 model is considered to be unsuitable for application to glaciomarine sediments
757 (Liu et al., 2019), whereas the ln(Zr/Rb) ratio is insensitive to such factors,
758 making it more suitable for characterising grain-size variations in Southern
759 Ocean sediments. In particular, we emphasise the strength of Zr/Rb ratios in
760 recording grain-size in the sortable fine fraction, whereas it appears that the
761 mean grain-size predictions from the multi-element approach also contain a
762 significant signal from the coarser sand fractions (DR Figure 4).

763 Despite these strengths, successful application of the ln(Zr/Rb) ratio as a
764 proxy for grain-size may also rely on sediment provenance being relatively
765 stable through time. This condition has presumably been met in the cores
766 discussed above (Table 1), but the sensitivity of Zr/Rb ratios to sediment
767 provenance remains to be fully explored. Importantly, we have shown that the
768 ln(Zr/Rb) ratio is insensitive to quartz-dominated IRD input at levels of up to
769 ~25 % and perhaps higher (Figs. 9B and 9E). Hence, its specificity to the

grain-size interval of interest for current transport supports the use of Zr/Rb ratios rather than the multi-element approach (Liu et al., 2019) for constraining grain-size in glaciomarine sediments. Nevertheless, we caution that the correlation between ln(Zr/Rb) and grain-size might be degraded if IRD accounts for a large majority of the sediment (e.g. within IRD layers) or if IRD is composed of Zr- and/or Rb-rich lithic grains. Particular care may be required for tephra-rich sediments, such as those found in the Antarctic Peninsula region (e.g. Toro et al., 2013). Tephra layers are typically characterised by high Zr (~180 ppm) and low Rb (~12 ppm) concentrations (Zhang and Liu, 1996), and hence could produce spikes in the Zr/Rb ratio and potentially decouple ln(Zr/Rb) from grain-size.

Some caution is also required when making core-to-core comparisons, especially for cores retrieved from different regions, because the value of ln(Zr/Rb) does not directly correspond to a specific value of a grain-size parameter. For example, differences in sediment provenance between regions or in machine detection efficiency (Eq. (3)) could lead to different relationships between absolute values of ln(Zr/Rb) and grain-size, even though the gradients appear constant (Figs. 12B-C). Such a scenario could also arise in long sediment cores (e.g. Toyos et al., 2020), for example if changes in climate, erosion, or paleogeography led to changes in provenance. Where only qualitative information is required, the ln(Zr/Rb) ratio may provide a convenient proxy for variations of grain-size in the silt fraction of glaciomarine sediment from the Southern Ocean without the need for additional measurements. However, for quantitative information and for effective comparisons between records from multiple cores, local calibrations between ln(Zr/Rb) and conventional grain-size data from a subset of coupled samples will be required. We also emphasise that for interpretations in terms of bottom current speed, high-resolution records of ln(Zr/Rb) must be combined with low-resolution grain-size records (SSM and SS%) in order to establish that the sediment is current-sorted (McCave and Andrews, 2019).

7 Summary and Conclusions

We conducted a range of grain-size measurements and Rb and Zr concentration measurements using both XRF core scanning and ICP-MS on four sediment cores retrieved from the Prydz Bay and Ross Sea regions. In combination with published data from two sediment cores in the Drake Passage region, we evaluated the use of ln(Zr/Rb) count ratios from XRF core scanning as a proxy for grain-size variations of glaciomarine sediment from the Southern Ocean.

Records of Rb and Zr counts from XRF core scanning are semi-quantitative due to specimen and matrix effects. However, by measuring Rb and Zr under the same conditions and using the ln(Zr/Rb) ratio, these effects can be accounted for. In this case, the ln(Zr/Rb) count ratio correlates well with the Zr/Rb concentration ratio measured by ICP-MS.

The ln(Zr/Rb) ratio mainly reflects the grain-size dependent composition of the sediment fractions that do not include coarse unsorted IRD, and therefore provides a proxy for the IRD-corrected mean grain-size of glaciomarine sediment from the Southern Ocean. The ln(Zr/Rb) ratio has a similar downcore pattern to SS% in all studied glaciomarine sediment cores, and hence can be used to indicate bottom current strength in cases where SS% and SSM are highly correlated. The link between ln(Zr/Rb) ratios and SS% could also be used to discriminate whether a SSM record reflects current sorting in cases where SS% data are unavailable. Based on all published Southern Ocean data, the regression line for SS% versus ln(Zr/Rb) appears to have a universal slope (34.1). In cases of bottom current sorting, such uniform slopes also appear to exist for SSM versus SS% (0.32), and for SSM versus ln(Zr/Rb) (12.7). The above correlation lines potentially provide a quick and convenient way to estimate the magnitude of changes in SS% and SSM (rather than absolute values) using only XRF scanning measurements of ln(Zr/Rb). However, caution will be required when ln(Zr/Rb) is applied to sediment that is dominated

by unsorted IRD or that is rich in Rb- and/or Zr-bearing IRD or tephra. In addition, ln(Zr/Rb) values cannot be directly compared between sediment cores from different regions, and local calibrations are required to obtain quantitative information on sediment grain-size.

Acknowledgements

We are grateful to the authors who have provided us with data on request or via online repositories. We thank the cruise members of the 29th, 30th, and 31st Chinese Antarctic Expedition for retrieving the sediments. This work was supported by National Natural Science Foundation of China (CN) and Postdoctoral Research Foundation of China (Grants No. 41806223, 2018M632158, 41776191 and 41676191).

Data availability

Supplementary data to this article can be found in the supporting information and will be available in PANGAEA repository.

References

Anderson, R.F., Ali, S., Bradtmiller, L.I., Nielsen, S.H.H., Fleisher, M.Q., Anderson, B.E., Burckle1, L.H., 2009. Wind-Driven Upwelling in the Southern Ocean and the Deglacial Rise in Atmospheric CO2. Science 323, 1443-1448.

Bostock, H.C., Barrows, T.T., Carter, L., Chase, Z., Cortese, G., Dunbar, G.B., Ellwood, M., Hayward, B., Howard, W., Neil, H.L., Noble, T.L., Mackintosh, A., Moss, P.T., Moy, A.D., White, D., Williams, M.J.M., Armand, L.K., 2013. A review of the Australian–New Zealand sector of the Southern Ocean over the last 30 ka (Aus-INTIMATE project). Quaternary Science Reviews 74, 35-57.

Bouchez, J., Gaillardet, J., France-Lanord, C., Maurice, L., Dutra-Maia, P., 2011. Grain size control of river suspended sediment geochemistry:

Clues from Amazon River depth profiles. Geochemistry, Geophysics, Geosystems 12, Q03008.

Budge, J., Long, D., 2018. A Comprehensive Database for Antarctic Iceberg Tracking Using Scatterometer Data. IEEE Journal of Selected Topics in Applied Earth Observations and Remote Sensing 11 1-9.

Chen, J., Chen, Y., Liu, L., Ji, J., Balsam, W., Sun, Y., Lu, H., 2006. Zr/Rb ratio in the Chinese loess sequences and its implication for changes in the East Asian winter monsoon strength. Geochimica et Cosmochimica Acta 70, 1471-1482.

Chen, Q., Kissel, C., Govin, A., Liu, Z., Xie, X., 2016. Correction of interstitial water changes in calibration methods applied to XRF core-scanning major elements in long sediment cores: Case study from the South China Sea. Geochemistry, Geophysics, Geosystems 17, 1925-1934.

Comiso, J., 2010. Variability and trends of the global sea ice cover. Sea Ice, Second Edition. Wiley-Blackwell. pp. 205-246.

DeConto, R.M., Pollard, D., 2016. Contribution of Antarctica to past and future sea-level rise. Nature 531, 591-597.

Dypvik, H., Harris, N.B., 2001. Geochemical facies analysis of fine-grained siliciclastics using Th/U, Zr/Rb and (Zr+Rb)/Sr ratios. Chemical Geology 181, 131-146.

Efron, B., Tibshirani, R.J., 1994. An Introduction to the Bootstrap (Chapman & Hall/CRC Monographs on Statistics & Applied Probability). Chapman and Hall/CRC.

Ehrmann, W.U., Melles, M., Kuhn, G., Grobe, H., 1992. Significance of clay mineral assemblages in the Antarctic Ocean. Marine Geology 107, 249-273.

Fralick, P., Kronberg, B.I., 1997. Geochemical discrimination of clastic sedimentary rock sources. Sedimentary Geology 113, 111-124.

Garcia, H.E., Locarnini, R.A., Boyer, T.P., 2009. Dissolved oxygen, apparent oxygen utilization, and oxygen saturation. World Ocean Atlas 3.

Gordon, A., Zambianchi, E., Orsi, A., Visbeck, M., Giulivi, C., Whitworth, T., Spezie, G., 2004. Energetic plumes over the western Ross Sea continental slope. Geophysical. Research. Letters. 31,L21302.

Guo, Y., Yang, S., Su, N., Li, C., Yin, P., Wang, Z., 2018. Revisiting the effects of hydrodynamic sorting and sedimentary recycling on chemical weathering indices. Geochimica et Cosmochimica Acta 227, 48-63.

Jaccard, S., Galbraith, E., Sigman, D., Haug, G., 2010. A pervasive link between Antarctic ice core and subarctic Pacific sediment records over the past 800 kyrs. Quaternary Science Reviews 29, 206-212.

Jaccard, S., Hayes, C.T., Martínez-García, A., Hodell, D., Anderson, R.F., Sigman, D., Haug, G., 2013. Two modes of change in Southern Ocean productivity over the past million years. Science 339, 1419-1423.

Jaccard, S.L., Galbraith, E.D., Martínez-García, A., Anderson, R.F., 2016. Covariation of deep Southern Ocean oxygenation and atmospheric CO_2 through the last ice age. Nature 530, 207-210.

Jansen, F., Gaast, S., Koster, B., Vaars, A., 1998. CORTEX, a shipboard XRF-scanner for element analyses in split sediment cores. Marine Geology 151, 143-153.

Jenkins, R., 2012. X-Ray Fluorescence Spectrometry, 2nd Edition. Wiley & Sons, New York. 207 pp.

Jiménez-Espejo, F., Presti, M., Kuhn, G., McKay, R., Crosta, X., Escutia, C., Lucchi, R., Tolotti, R., Yoshimura, T., Huertas, M., Macrì, P., Caburlotto, A., Santis, L., 2019. Late Pleistocene oceanographic and depositional variations along the Wilkes Land margin (East Antarctica) reconstructed with geochemical proxies in deep-sea sediments. Global and Planetary Change, 103045.

Jin, Z.D., Li, F., Cao, J., Wang, S., Yu, J., 2006. Geochemistry of Daihai Lake sediments, Inner Mongolia, north China: Implications for provenance, sedimentary sorting, and catchment weathering. Geomorphology 80, 147-163.

Jonkers, L., Barker, S., Hall, I.R., Prins, M.A., 2015. Correcting for the influence of ice-rafted detritus on grain size-based paleocurrent speed estimates. Paleoceanography 30, 1347-1357.

Jung, H., Lim, D., Jeong, D., Xu, Z., Li, T., 2016. Discrimination of sediment provenance in the Yellow Sea: Secondary grain-size effect and REE proxy. Journal of Asian Earth Sciences 123, 78-84.

Konert, M., Vandenberghe, J., 1997. Comparison of laser grain size analysis with pipette and sieve analysis: a solution for the underestimation of the clay fraction. Sedimentology 44, 523-535.

Lamy, F., Arz, H.W., Kilianc, R., Lange, C.B., Lembke-Jene, L., Wengler, M., Kaiser, J., Baeza-Urrea, O., Hall, I.R., Harada, N., Tiedemann, R., 2015. Glacial reduction and millennial-scale variations in Drake Passage throughflow. Proceedings of the National Academy of Sciences of the United States of America 112, 13496-13501.

Lamy, F., Gersonde, R., Winckler, G., Esper, O., Jaeschke, A., Kuhn, G., Ullermann, J., Martinez-Garcia, A., Lambert, F., Kilian, R., 2014. Increased Dust Deposition in the Pacific Southern Ocean During Glacial Periods. Science 343, 403-407.

Li, G., Piper, D.J.W., 2015. The influence of meltwater on the labrador current in Heinrich event 1 and the younger Dryas. Quaternary Science Reviews 107, 129-137.

Lisiecki, L.E., Raymo, M.E., 2005. A Pliocene‐Pleistocene stack of 57 globally distributed benthic δ18O records. Paleoceanography 20, PA1003.

Liu, D., Bertrand, S., Weltje, G., 2019. An Empirical Method to Predict Sediment Grain Size From Inorganic Geochemical Measurements. Geochemistry, Geophysics, Geosystems. 20, 3690-3704.

Liu, L., Chen, J., Chen, Y., Ji, J., Lu, H., 2002. Variation of Zr/Rb ratios on the Loess Plateau of Central China during the last 130000 years and its implications for winter monsoon. Chinese Science Bulletin 47,

1298-1302.

Liu, L., Chen, J., Ji, J., Chen, Y., 2004. Comparison of paleoclimatic change from Zr/Rb ratios in Chinese loess with marine isotope records over the 2.6–1.2 Ma BP interval. Geophysical Research Letters 31, L15204,.

Lyle, M., Backman J., 2013. Data report: Calibration of XRF-estimated CaCO3 along the Site U1338 splice, in Proceedings of IODP, 320/321, edited by H. P€alike et al., Integrated Ocean Drill. Program Manage. Int., Inc., Tokyo, 349–360, doi:10.2204/iodp.proc.320321.205.2013.

Lyle, M., A. O. Lyle, T. Gorgas, A. Holbourn, T. Westerhold, E. Hathorne, K. Kimoto, and S. Yamamoto, 2012. Data report: Raw and normalized elemental data along the Site U1338 splice from X-ray flfluorescence scanning, in Proceedings of IODP, 320/321, edited by H. P€alikeet al., Integrated Ocean Drill. Program Manage. Int., Inc., Tokyo.

Mao, L., Piper, D.J.W., Saint-Ange, F., Andrews, J.T., 2018. Labrador Current fluctuation during the last glacial cycle. Marine Geology 395, 234-246.

Marshall, J., Speer, K., 2012. Closure of the meridional overturning circulation through Southern Ocean upwelling. Nature Geoscience 5, 171-180.

Marshall, N., Piper, D., Saint-Ange, F., Campbell, D., 2014. Late Quaternary history of contourite drifts and variations in Labrador Current flow, Flemish Pass, offshore eastern Canada. Geo-Marine Letters 34, 457-470.

Mathiot, P., Goosse, H., Fichefet, T., Barnier, B., Gallée, H., 2011. Modelling the seasonal variability of the Antarctic Slope Current. Ocean Science 7, 445-532.

McCave, I., 2008. Size sorting during transport and deposition of fine sediments: sortable silt and flow speed. Contourites. Developments in Sedimentology 60, 121-142.

McCave, I., Andrews, J., 2019. Distinguishing current effects in sediments delivered to the ocean by ice. I. Principles, methods and examples. Quaternary Science Reviews 212, 92-107.

McCave, I., Hall, I., Bianchi, G., 2006. Laser vs. settling velocity differences in silt grainsize measurements: Estimation of palaeocurrent vigour. Sedimentology 53, 919-928.

McCave, I.N., Crowhurst, S.J., Kuhn, G., Hillenbrand, C.D., Meredith, M.P., 2014. Minimal change in Antarctic Circumpolar Current flow speed between the last glacial and Holocene. Nature Geoscience 7, 113-116.

McCave, I.N., Manighetti, B., Robinson, S.G., 1995. Sortable silt and fine sediment size composition slicing-parameters for paleocurrent speed and paleoceanography. Paleoceanography 10, 593-610.

McCave, I.N., Thornalley, D.J.R., Hall, I.R., 2017. Relation of sortable silt grain-size to deep-sea current speeds: Calibration of the 'Mud Current Meter'. Deep Sea Research Part I: Oceanographic Research Papers 127, 1-12.

Meijers, A.J.S., Klocker, A., Bindoff, N.L., Williams, G.D., Marsland, S.J., 2010. The circulation and water masses of the Antarctic shelf and continental slope between 30 and 80◦E. Deep Sea Research Part II: Topical Studies in Oceanography 57, 723-737.

Orsi, A.H., Whitworth, T., 2005. Hydrographic Atlas of the world ocean circulation experiment. In: Sparrow, M., Chapman, P., Gould, J. (Eds.), Southern Ocean, vol. 1. International WOCE Project Office, Southampton, U.K, ISBN 0-904175-49-9.

Orsi, A.H., Whitworth, T., Nowlin, W.D., 1995. On the meridional extent and fronts of the Antarctic Circumpolar Current. Deep Sea Research Part I: Oceanographic Research Papers 42, 641-673.

Passchier, S., 2011, Linkages between East Antarctic Ice Sheet extent and Southern Ocean temperatures based on a Pliocene high-resolution record of ice-rafted debris off Prydz Bay, East Antarctica: Paleoceanography, v. 26, no. 4, PA4204

Pettijohn, F.J., 1941. Persistence of Heavy Minerals and Geologic Age. The Journal of Geology 49, 610-625.

Presti, M., Barbara, L., Denis, D., 2011. Sediment delivery and depositional patterns off Adélie Land (East Antarctica) in relation to late Quaternary climatic cycles. Marine Geology 284, 96-113.

Richter, T.O., Van der Gaast, S., Koster, B., Vaars, A., Gieles, R., de Stigter, H.C., De Haas, H., van Weering, T.C., 2006. The Avaatech XRF Core Scanner: technical description and applications to NE Atlantic sediments. Geological Society, London, Special Publications 267, 39-50.

Rintoul, S., Speer, K., Sparrow, M., Meredith, M., Hofmann, E., Fahrbach, E., Summerhayes, C., Fukamachi, Y., Garabato, A., Alverson, K., Ryabinin, V., 2010. “Southern ocean observing system (SOOS): rationale and strategy for sustained observations of the Southern Ocean,” in Proceedings of OceanObs ‘09: Sustained Ocean Observations and Information for Society. (Venice).

Schlitzer, R., 2009. Ocean Data View Software. http://odv.awi.de/

Schloesser, F., Friedrich, T., Timmermann, A., DeConto, R., Pollard, D., 2019. Antarctic iceberg impacts on future Southern Hemisphere climate. Nature Climate Change 9, 672-677.

Sigman, D.M., Hain, M.P., Haug, G.H., 2010. The polar ocean and glacial cycles in atmospheric CO2 concentration. Nature 466, 47-55.

Tang, Z., Shi, X., Zhang, X., Chen, Z., Chen, M.-T., Wang, X., Wang, H., Liu, H., Lohmann, G., Li, P., Ge, S., Huang, Y., 2016. Deglacial biogenic opal peaks revealing enhanced Southern Ocean upwelling during the last 513 ka. Quaternary International 425, 445-452.

Taviani, M., Reid, D., Anderson, J., 1993. Skeletal and isotopic composition and paleoclimatic significance of Late Pleistocene carbonates, Ross Sea, Antarctica. Journal of Sedimentary Research 63, 84-90.

Taylor, S.R., 1965. The application of trace element data to problems in petrology. Physics and Chemistry of the Earth 6, 133-213.

Teitler, L., Warnke, D.A., Venz, K.A., Hodell, D.A., Becquey, S., Gersonde, R., Teitler, W., 2010. Determination of Antarctic Ice Sheet stability over the

last ~500 ka through a study of iceberg-rafted debris. Paleoceanography 25, PA1202.

Tian, J., Xie, X., Ma, W., Jin, H., Wang, P., 2011. X-ray fluorescence core scanning records of chemical weathering and monsoon evolution over the past 5 Myr in the southern South China Sea. paleoceanography 26, PA4202,

Tjallingii, R., Röhl, U., Kölling, M., Bickert, T., 2007. Influence of the water content on X-ray fluorescence core-scanning measurements in soft marine sediments. Geochemistry, Geophysics, Geosystems 8, 1-16.

Toro, M., Granados, I., Pla, S., Giralt, S., Antoniades, D., Galán, L., Cortizas, A., Lim, H.S., Appleby, P., 2013. Chronostratigraphy of the sedimentary record of Limnopolar Lake, Byers Peninsula, Livingston Island, Antarctica. Antarctic Science 25, 198-212.

Toyos, M.H., Lamy, F., Lange, C.B., Lembke-Jene, L., Saavedra-Pellitero, M., Esper, O., Arz, H.W., 2020. Antarctic Circumpolar Current Dynamics at the Pacific Entrance to the Drake Passage Over the Past 1.3 Million Years. Paleoceanography and Paleoclimatology 35, e2019PA003773.

Vries, J.L., Vrebos, B., 2002. Quantification of infinitely thick specimens by XRF analysis. Handbook of X-Ray Spectrometry, 341-405.

Weber, M.E., Clark, P.U., Kuhn, G., Timmermann, A., Sprenk, D., Gladstone, R., Zhang, X., Lohmann, G., Menviel, L., Chikamoto, M.O., Friedrich, T., Ohlwein, C., 2014. Millennial-scale variability in Antarctic ice-sheet discharge during the last deglaciation. Nature 510, 134-138.

Weber, M.E., Kuhn, G., Sprenk, D., Rolf, C., Ohlwein, C., Ricken, W., 2012. Dust transport from Patagonia to Antarctica-A new stratigraphic approach from the Scotia Sea and its implications for the last glacial cycle. Quaternary Science Reviews 36, 177-188.

Wei, G.J., Liu, Y., Li, X.H., Shao, L., Liang, X.R., 2003. Climatic impact on Al, K, Sc and Ti in marine sediments: Evidence from ODP Site 1144, South China Sea. Geochemical Journal 37, 593-602.

Weltje, G., Bloemsma, M., Tjallingii, R., Heslop, D., Röhl, U., Croudace, I., 2015. Prediction of Geochemical Composition from XRF Core Scanner Data: A New Multivariate Approach Including Automatic Selection of Calibration Samples and Quantification of Uncertainties, in Micro-XRF Studies of Sediment Cores: Applications of a non-destructive tool for the environmental sciences, edited by W. I. Croudace and G. R. Rothwell. Springer, Dordrecht, Netherlands, pp. 507-534.

Weltje, G.J., Tjallingii, R., 2008. Calibration of XRF core scanners for quantitative geochemical logging of sediment cores: Theory and application. Earth and Planetary Science Letters 274, 423-438.

Williams, T., van de Flierdt, T., Hemming, S.R., Chung, E., Roy, M., Goldstein, S.L., 2010. Evidence for iceberg armadas from East Antarctica in the Southern Ocean during the late Miocene and early Pliocene. Earth and Planetary Science Letters 290, 351-361.

Wilson, D., Bertram, R., Needham, E., van de Flierdt, T., Welsh, K., McKay, R., Mazumder, A., Riesselman, C., Jiménez-Espejo, F., Escutia, C., 2018. Ice loss from the East Antarctic Ice Sheet during late Pleistocene interglacials. Nature 561, 383-386.

Wilson, D., Struve, T., van de Flierdt, T., Chen, T., Li, T., Burke, A., Robinson, L., 2020. Sea-ice control on deglacial lower cell circulation changes recorded by Drake Passage deep-sea corals. Earth and Planetary Science Letters 544, 116405.

Wu, L., Krijgsman, W., Liu, J., Li, C., Wang, R., Xiao, W., 2020. CFLab: A MATLAB GUI program for decomposing sediment grain size distribution using Weibull functions. Sedimentary Geology 398, 105590.

Wu, L., Wang, R., Krijgsman, W., Chen, Z., Xiao, W., Ge, S., Wu, J., 2019. Deciphering Color Reflectance Data of a 520-kyr Sediment Core From the Southern Ocean: Method Application and Paleoenvironmental Implications. Geochemistry, Geophysics, Geosystems 20, 2808-2826.

Wu, L., Wang, R., Xiao, W., Ge, S., Chen, Z., Krijgsman, W., 2017.

Productivity-climate coupling recorded in Pleistocene sediments off Prydz Bay (East Antarctica). Palaeogeography, Palaeoclimatology, Palaeoecology 485, 260-270.

Wu, L., Wang, R., Xiao, W., Krijgsman, W., Li, Q., Ge, S., Ma, T., 2018. Late Quaternary Deep Stratification-Climate Coupling in the Southern Ocean: Implications for Changes in Abyssal Carbon Storage. Geochemistry, Geophysics, Geosystems 19 (2). 379-395.

Yabuki, T., Suga, T., Hanawa, K., Matsuoka, K., Kiwada, H., Watanabe, T., 2006. Possible source of the antarctic bottom water in the Prydz Bay region. Journal of Oceanography 62, 649-655.

Yang, S., Jung, H., Choi, M., Li, C., 2002. The rare earth element compositions of the Changjiang (Yangtze) and Huanghe (Yellow) river sediments. Earth and Planetary Science Letters 201, 407-419.

Yokoyama, Y., Anderson, J.B., Yamane, M., Simkins, L.M., Miyairi, Y., Yamazaki, T., Koizumi, M., Suga, H., Kusahara, K., Prothro, L., Hasumi, H., Southon, J.R., Ohkouchi, N., 2016. Widespread collapse of the Ross Ice Shelf during the late Holocene. Proceedings of the National Academy of Sciences 113, 2354-2359.

Zhang, W., Liu, J., 1996. The composition of Volcanic Ash from ice core of Collins Cap, King George Island of Antarctica (In Chinese with English abstract). Acta Petrologica Sinica 12, 434-445.

Ziegler, M., Jilbert, T., De Lange, G.J., Lourens, L.J., Reichart, G.J., 2008. Bromine counts from XRF scanning as an estimate of the marine organic carbon content of sediment cores. Geochemistry Geophysics Geosystems 9 (5), 1-6.

Table Caption

Table 1 Information on sediment cores used and referred to in this study

Figure captions

Fig. 1 Environmental setting of the study area. (A) The Southern Ocean and the studied core sites. The ocean frontal system is after Orsi, et al. (1995) and Bostock et al. (2013). SACCF: Southern Antarctic Circumpolar Current Front; PF: Polar Front; SAF: Subantarctic Front; STF: Subtropical Front. (B) The Prydz Bay area. LGAISS: Lambert Glacier-Amery Ice Shelf system. (C) The Ross Sea area. See Table 1 for locations of the cores sites. Figure plotted in Ocean Data View (Schlitzer, 2009).

Fig. 2 Downcore records from Prydz Bay core P1-2 plotted versus age. (A) Rb counts and concentration. (B) Zr counts and concentration. (C) Zr/Rb count ratio from XRF core scanning and Zr/Rb concentration ratio from ICP-MS. (D) Mean grain-size (samples with extremely high grain-size plotted in red). (E) SSM and SS%. (F) Spectrum of grain-size compositions. Glacial intervals are shaded grey and labelled with MIS numbers according to Lisiecki and Raymo (2005).

Fig. 3 Downcore records from Ross Sea core JB06 plotted versus depth. (A) Water content (note reversed axis). (B) Rb counts from XRF scanning. (C) Zr counts from XRF scanning. (D) Zr/Rb count ratio from XRF scanning. (E) Mean grain-size. (F) SSM and SS%. (G) Spectrum of grain-size compositions. Dashed lines in (D) and (E) indicate the general decreasing trends towards the core top. The yellow shading indicates a layer rich in benthic foraminifera

Cassidulina sp. of last glacial age (< 36 ka ^{14}C age according to Taviani et al. (1993) and Yokoyama et al. (2016)).

Fig. 4 Time series derived from XRF scanning of (A) Rb counts, (B) Zr counts, and (C) ln(Zr/Rb) count ratios from Prydz Bay sediment cores P1-2, P1-3, and P4-1. Glacial intervals are shaded grey and labelled with MIS numbers according to Lisiecki and Raymo (2005)

Fig. 5 Results of grain-size separation experiment on cores P1-2 and JB06. Distribution of (A) Rb concentration, (B) Zr concentration, and (C) Zr/Rb concentration ratios against grain-size. All data were measured by ICP-MS.

Fig. 6 Scatter plots for core P1-2 of (A) Rb concentration versus Rb counts, (B) Zr concentration versus Zr counts, (C) ln(Zr/Rb) concentration ratio versus ln(Zr/Rb) count ratio, (D) Zr/Rb concentration ratio versus ln(Zr/Rb) concentration ratio, and (E) Zr/Rb concentration ratio versus ln(Zr/Rb) count ratio. The count data were derived from XRF core scanning and the concentration data from ICP-MS measurement.

Fig. 7 Bootstrap test on the robustness of the calibration between ln(Zr/Rb) count ratios (from XRF core scanning) and Zr/Rb concentration ratios (from ICP-MS) (Fig. 6E). (A) and (B) Probability distributions of slope α and intercept β in Eq. (6). (C) Measured Zr/Rb concentrations in core P1-2 (ICP-MS data) compared to estimates based on the calibration of XRF scanning data. Glacial intervals in (C) are shaded grey and labelled with MIS numbers according to Lisiecki and Raymo (2005).

Fig. 8 Correlation relationship between the ln(Zr/Rb) count ratio and grain-size from sediment cores P1-2 and JB06. (A) and (B) Spectra of the correlation coefficient between the ln(Zr/Rb) count ratio and the volume percent of

sediment in each grain-size bin from cores P1-2 and JB06, respectively. (C) and (D) Spectra of the correlation coefficient between the ln(Zr/Rb) count ratio and the partial mean grain-size (PMG) in cores P1-2 and JB06, respectively. The ln(Zr/Rb) count ratio was derived from XRF core scanning. Coloured dots indicate correlation coefficients that are statistically significant (red) or insignificant (black) relative to the 1% confidence level.

Fig. 9 Scatter plots of (A) mean grain-size versus volume percent of the >63 μm fraction in core P1-2, (B) ln(Zr/Rb) from XRF scanning versus volume percent of the >63 μm fraction in core P1-2, (C) SSM versus volume percent of the >63 μm fraction in core P1-2, (D) mean grain-size versus volume percent of the >100 μm fraction in core JB06, (E) ln(Zr/Rb) from XRF core scanning versus volume percent of the >100 μm fraction in core JB06, and (F) SSM versus volume percent of the >100 μm fraction in core JB06.

Fig. 10 Time series of grain-size parameters relating to ln(Zr/Rb) in core P1-2. (A) PMG_{63}. (B) Ratio of the volume percent in the 7-63 μm fraction and the <6 μm fraction. (C) SS%. (D) SSM. (E) ln(Zr/Rb) count ratio from XRF core scanning. Glacial intervals are shaded grey and labelled with MIS numbers according to Lisiecki and Raymo (2005).

Fig. 11 Downcore record of grain-size parameters relating to ln(Zr/Rb) in core JB06. (A) PMG_{100}. (B) Ratio of the volume percent in the 30-100 μm fraction and the <23 μm fraction. (C) SS%. (D) SSM. (E) ln(Zr/Rb) count ratio from XRF core scanning. The yellow shading indicates a layer rich in benthic foraminifera *Cassidulina sp.* of last glacial age (< 36 ka ^{14}C age according to Taviani et al. (1993) and Yokoyama et al. (2016)).

Fig. 12 Scatter plots of (A) SSM versus SS%, (B) SS% versus XRF ln(Zr/Rb), (C) SSM versus XRF ln(Zr/Rb), (D) SSM_N versus $SS\%_N$, (E) $SS\%_N$ versus

XRF $\ln(Zr/Rb)_N$, (F) SSM_N versus XRF $\ln(Zr/Rb)_N$. The parameters $SS\%_N$, SSM_N, and XRF $\ln(Zr/Rb)_N$ are the values after subtracting their respective means. In the legends, S is the slope of regression lines and R is the correlation coefficient. In (E), the S and R values were calculated based on all core data. In (D) and (F), the S and R values were calculated based on data from cores JB06, 3128, and 93-2. See Table 1 for core locations and references. Note that the grain-size from these cores were measured by different methods, i.e. grain-size from core P1-2 and JB06 were measured using an Automatic Laser Analyzer (Beckman Coulter LS230) (Wu et al., 2018), grainsize from cores 3128 and 93-2 were measured by a Micromeritics SediGraph 5100. Data from MIS 1, 5, and 11 in core 93-2 are anomalous and not plotted (see Toyos et al., 2020).

Table 1 Information on sediment cores used and referred to in this study

Site	Label	Longitude (°E)	Latitude (°S)	Water depth (m)	Core length (cm)	Data source
ANT30/P1-02	P1-2	72.94	65.01	2860	624	This study; Wu et al. (2017, 2018, 2019)
ANT30/P1-03	P1-3	73.02	65.99	2542	599	This study; Wu et al. (2017); Tang et al. (2016)
ANT29/P4-01	P4-1	70.69	64.94	3162	421	This study; Wu et al. (2017)
ANT31/JB06	JB06	173.91	74.47	567.5	299	This study
MD07-3128	3128	-75.57	52.66	1032	-	Lamy et al. (2015)
PS97/093-2	93-2	-70.37	57.5	3781	-	Toyos et al. (2020)

Figure 1.

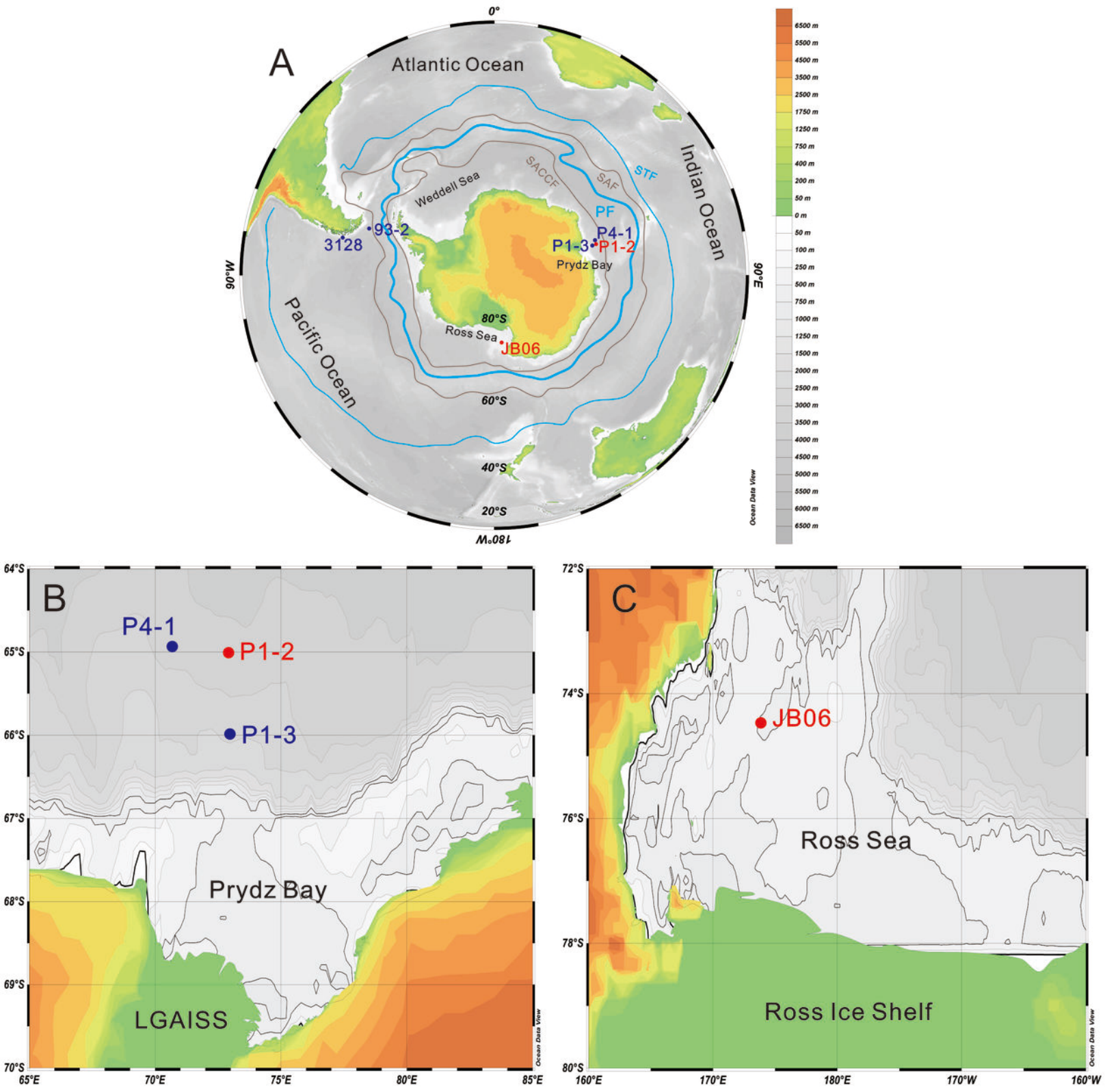
A
Atlantic Ocean
Indian Ocean
Pacific Ocean
Weddell Sea
Ross Sea
Prydz Bay
SACCF
SAF
STF
PF
3128
93-2
P4-1
P1-3
P1-2
JB06
0°
90°W
90°E
180°W
80°S
60°S
40°S
20°S
6500 m
5500 m
4500 m
3500 m
2500 m
1750 m
1250 m
750 m
400 m
200 m
50 m
0 m
50 m
100 m
250 m
500 m
750 m
1000 m
1250 m
1500 m
2000 m
2500 m
3000 m
3500 m
4000 m
4500 m
5000 m
5500 m
6000 m
6500 m
Ocean Data View
B
P4-1
P1-2
P1-3
Prydz Bay
LGAISS
64°S
65°S
66°S
67°S
68°S
69°S
70°S
65°E
70°E
75°E
80°E
85°E
Ocean Data View
C
JB06
Ross Sea
Ross Ice Shelf
72°S
74°S
76°S
78°S
80°S
160°E
170°E
180°E
170°W
160°W
Ocean Data View

Figure 2.

MIS 2 4 6 8 10 12

A

XRF Rb (counts/30 s)

ICP-MS Rb (ppm)

B

XRF Zr (counts/30 s)

ICP-MS Zr (ppm)

C

XRF Zr/Rb

ICP-MS Zr/Rb

D

Mean grain-size (μm)

E

SSM (μm)

SS%

F

Grain-size (μm)

Volume (%)

Age (ka)

Figure 3.

A

B

C

D

E

F

G

XRF Rb (counts/30 s)

Water Content (wt. %)

XRF Zr (counts/30 s)

XRF Zr/Rb

Mean grain-size (µm)

SSM (µm)

SS% (%)

Grain-size (µm)

Volume (%)

Depth (cm)

Figure 4.

MIS 2 4 6 8 10 12

P1-2
P1-3
P4-1

A

XRF Rb (counts/30 s)

6000
5000
4000
3000

B

XRF Zr (counts/30 s)

10000
8000
6000
4000

C

XRF ln(Zr/Rb)

0.8
0.6
0.4
0.2
0
-0.2

0 50 100 150 200 250 300 350 400 450 500

Age (ka)

Figure 5.

A

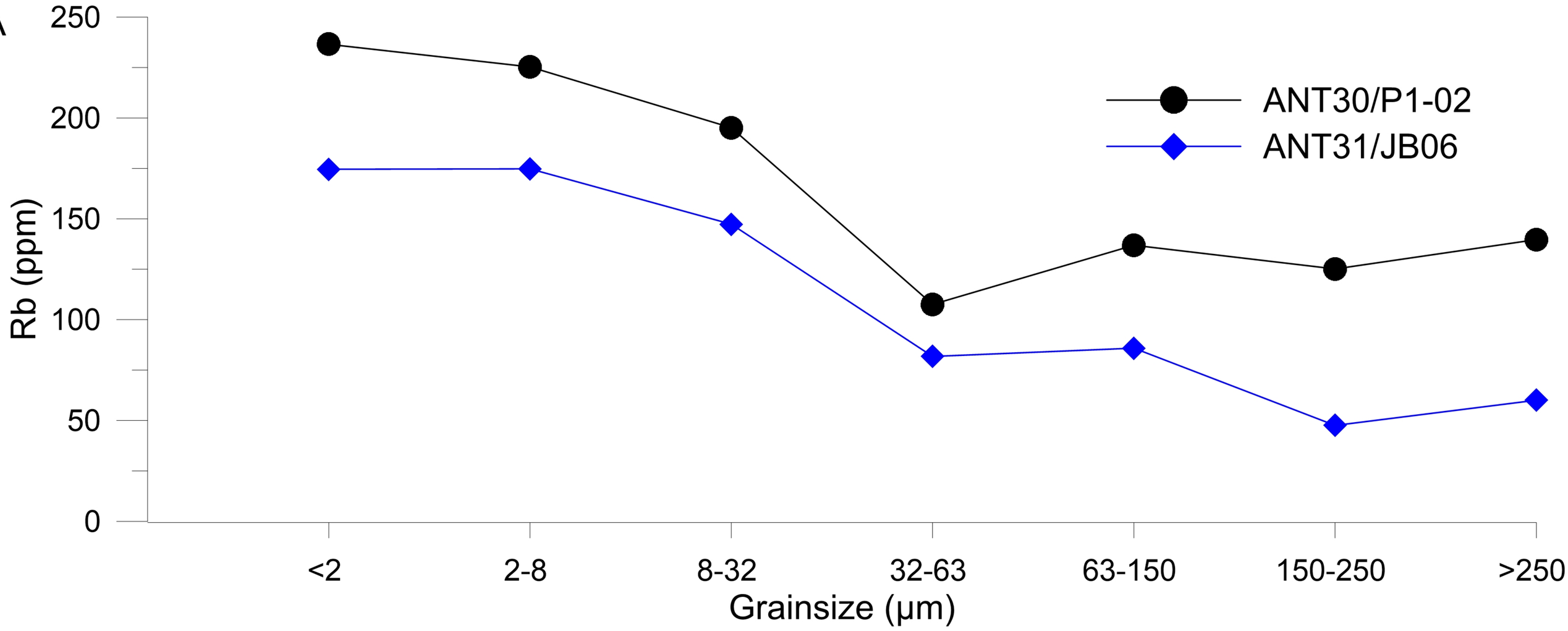
250
200
150
100
50
0
Rb (ppm)
ANT30/P1-02
ANT31/JB06
<2
2-8
8-32
32-63
63-150
150-250
>250
Grainsize (µm)

B

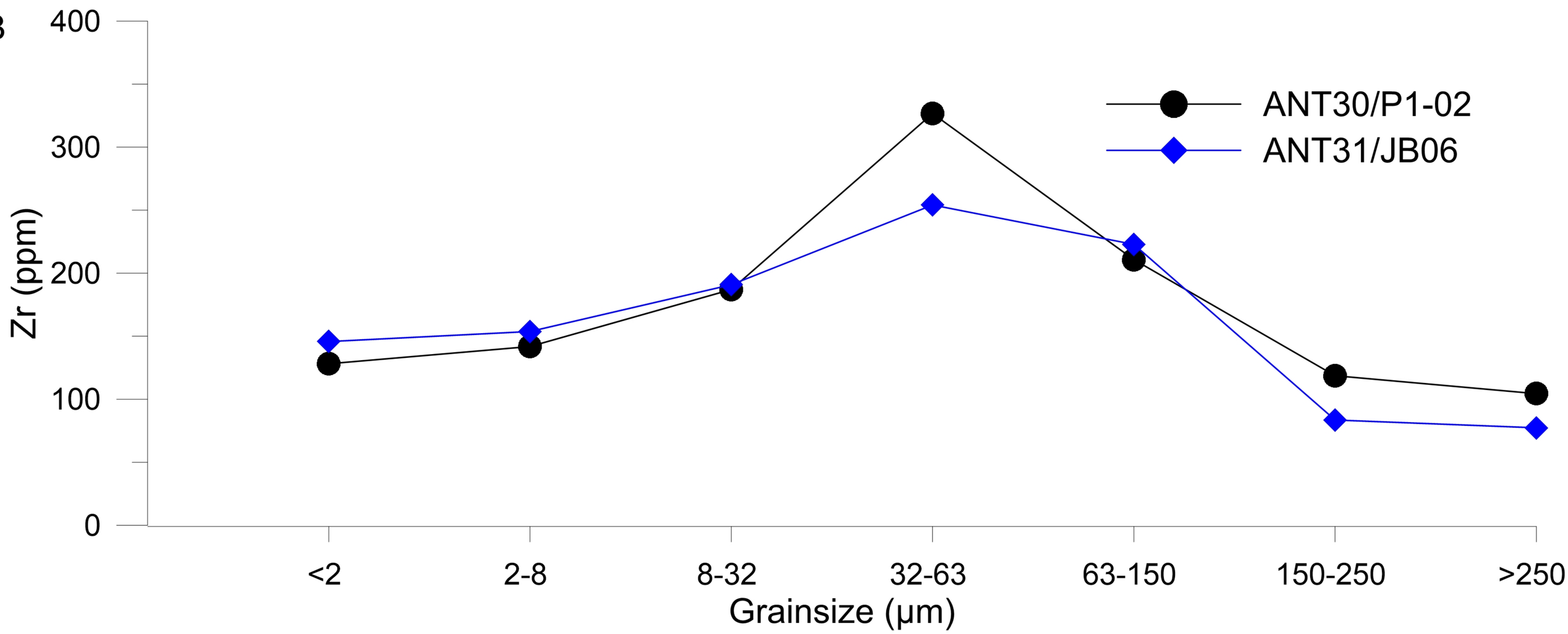
400
300
200
100
0
Zr (ppm)
ANT30/P1-02
ANT31/JB06
<2
2-8
8-32
32-63
63-150
150-250
>250
Grainsize (µm)

C

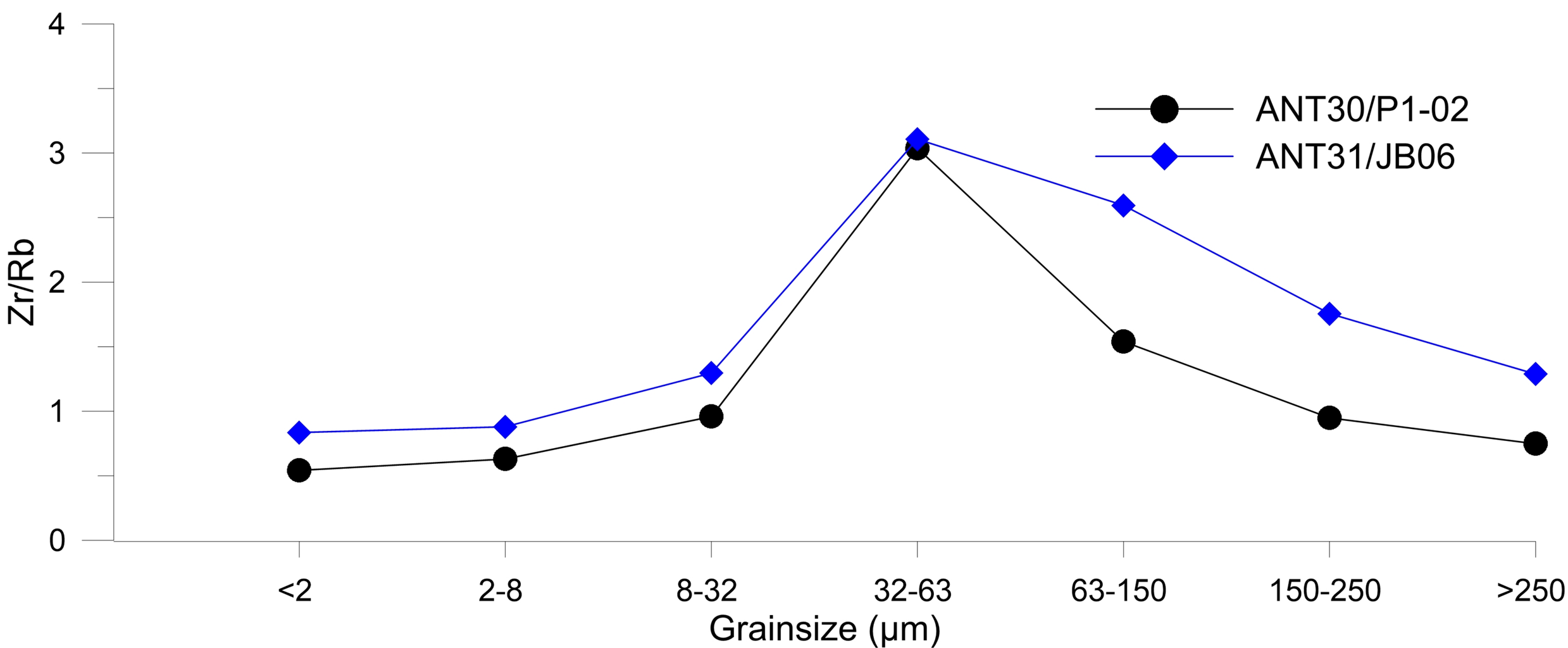
4
3
2
1
0
Zr/Rb
ANT30/P1-02
ANT31/JB06
<2
2-8
8-32
32-63
63-150
150-250
>250
Grainsize (µm)

Figure 6.

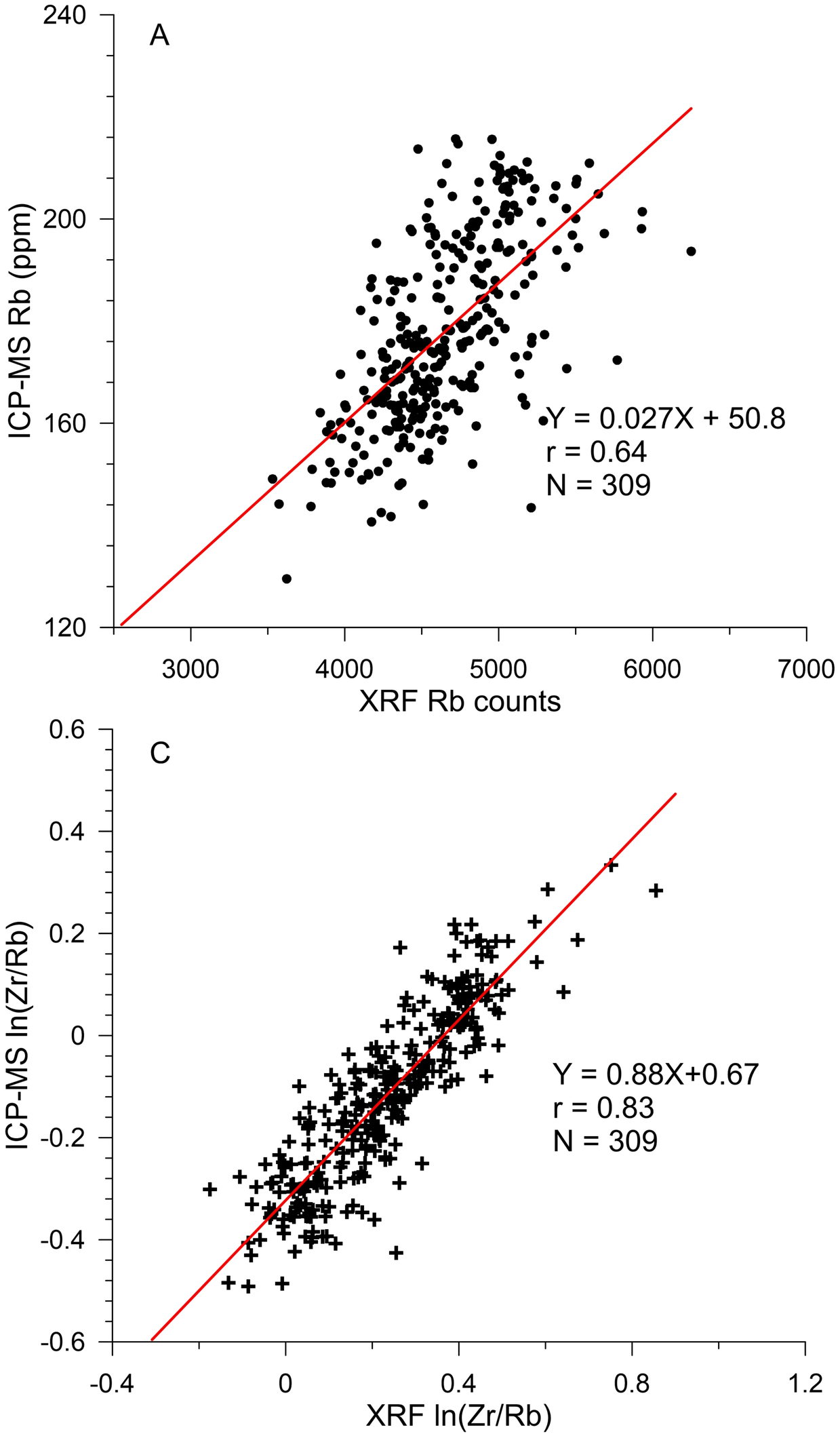
A
ICP-MS Rb (ppm)
XRF Rb counts
Y = 0.027X + 50.8
r = 0.64
N = 309

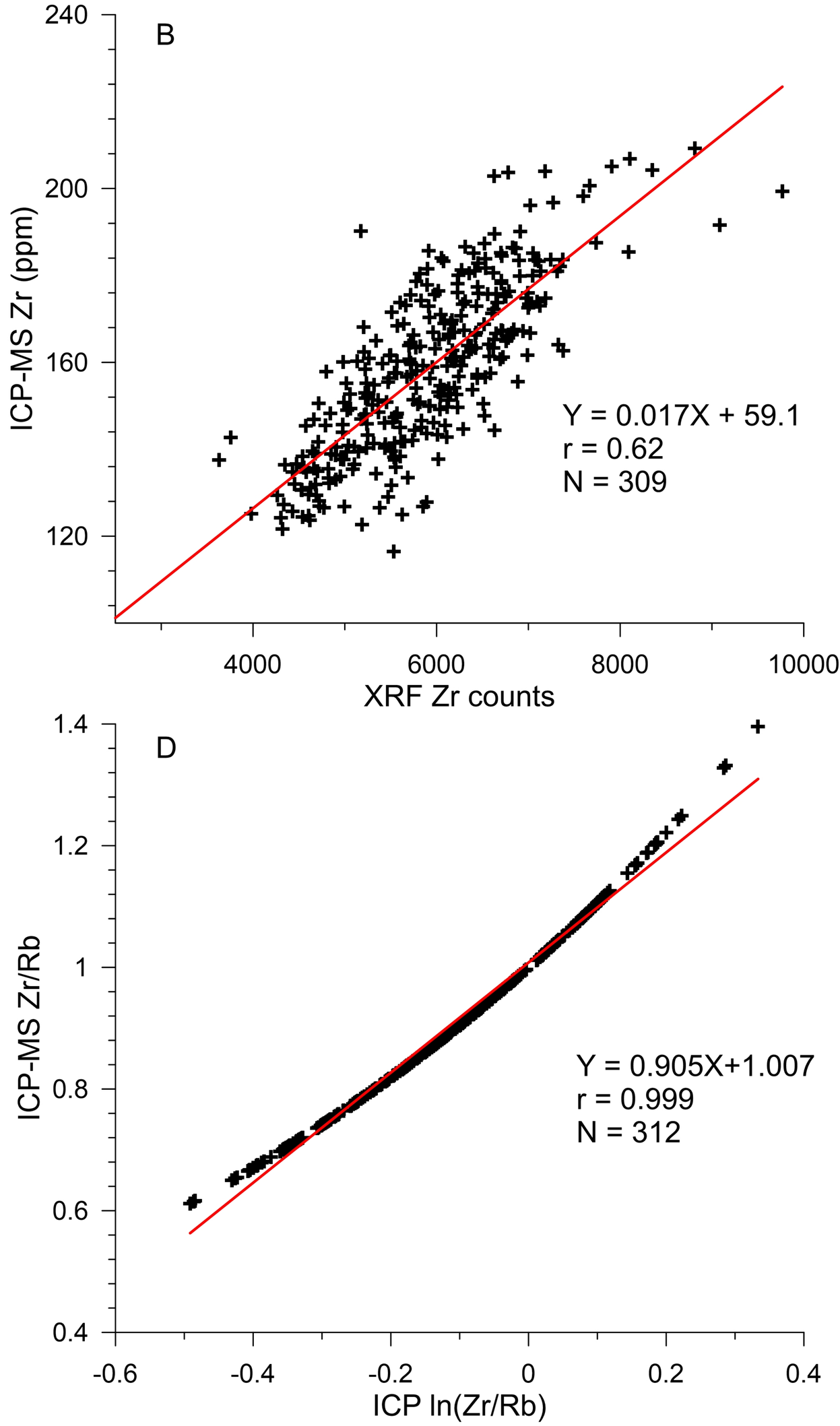
B
ICP-MS Zr (ppm)
XRF Zr counts
Y = 0.017X + 59.1
r = 0.62
N = 309

C
ICP-MS ln(Zr/Rb)
XRF ln(Zr/Rb)
Y = 0.88X+0.67
r = 0.83
N = 309

D
ICP-MS Zr/Rb
ICP ln(Zr/Rb)
Y = 0.905X+1.007
r = 0.999
N = 312

E
ICP-MS Zr/Rb
XRF-Ln（Zr/Rb)
Y = 0.79X + 0.72
r = 0.88
N = 309

Figure 7.

A

μ = 1.08
σ = 0.11
N = 10000

Probability

0.25
0.2
0.15
0.1
0.05
0

0.8 0.9 1 1.1 1.2 1.3 1.4 1.5 1.6 1.7 1.8

α

B

μ = -0.37
σ = 0.03
N = 10000

Probability

0.2
0.16
0.12
0.08
0.04
0

-0.52 -0.48 -0.44 -0.4 -0.36 -0.32 -0.28 -0.24

β

C

Zr/Rb concentration ratio

0.5 1 1.5 2

Age (ka)

0 50 100 150 200 250 300 350 400 450 500

2 4 6 8 10 12

MIS

ICP-MS measurement
Bootstrap mean
Bootstrap ±2σ range
Bootstrap Min-Max range

Figure 8.

A

ANT30/P1-02

Average grain-size distribution

r (sig. > 0.01)

r (sig. < 0.01)

Clay

Silt

Sand

r

Volume (%)

Grain-size (µm)

B

ANT31/JB06

Average grain-size distribution

r (sig. > 0.01)

r (sig. < 0.01)

Clay

Silt

Sand

r

Volume (%)

Grain-size (µm)

C

ANT30/P1-02

Average cumulative grain-size distribution

r (sig. > 0.01)

r (sig. < 0.01)

Clay

Silt

Sand

r

Volume (%)

Grain-size (µm)

D

ANT31/JB06

Average cumulative grain-size distribution

r (sig. > 0.01)

r (sig. < 0.01)

Clay

Silt

Sand

r

Volume (%)

Grain-size (µm)

Figure 9.

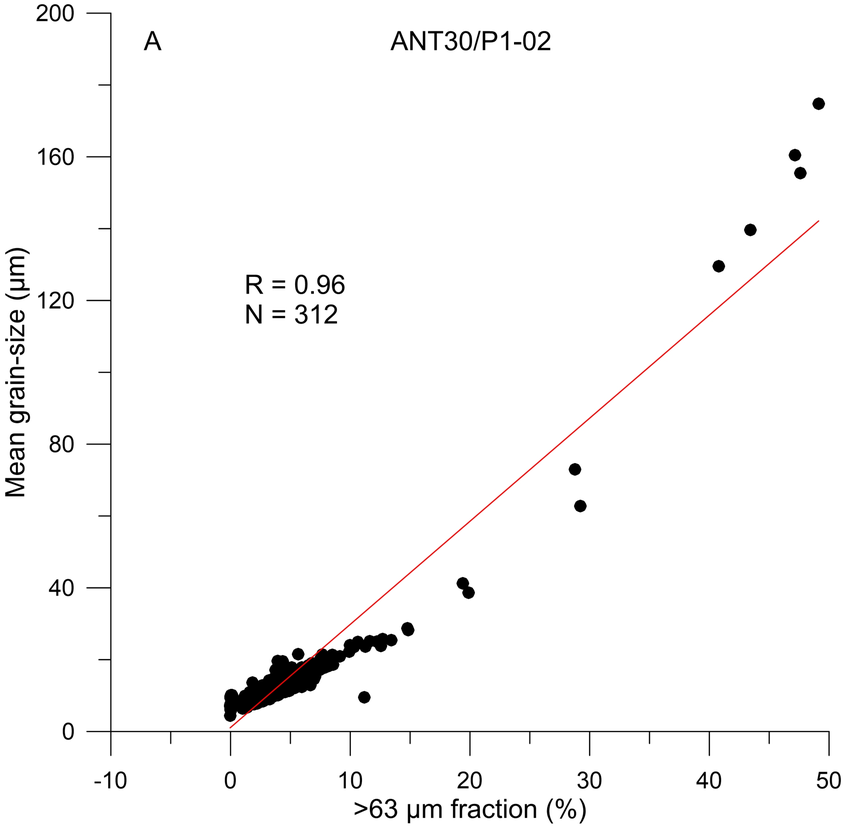
A
ANT30/P1-02
R = 0.96
N = 312
Mean grain-size (µm)
>63 µm fraction (%)

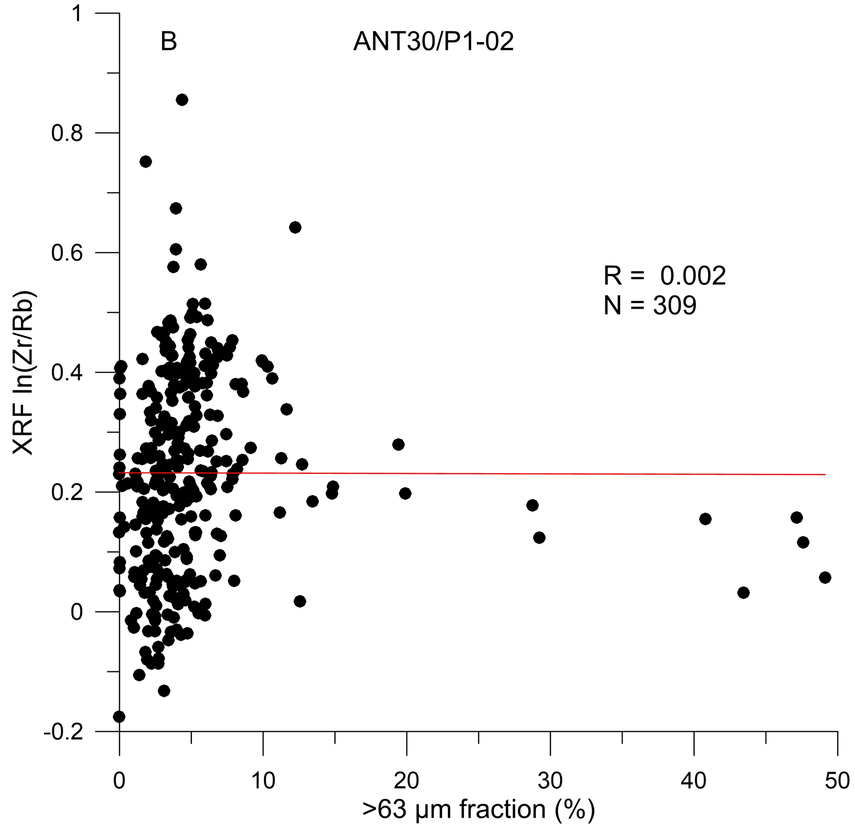
B
ANT30/P1-02
R = 0.002
N = 309
XRF ln(Zr/Rb)
>63 µm fraction (%)

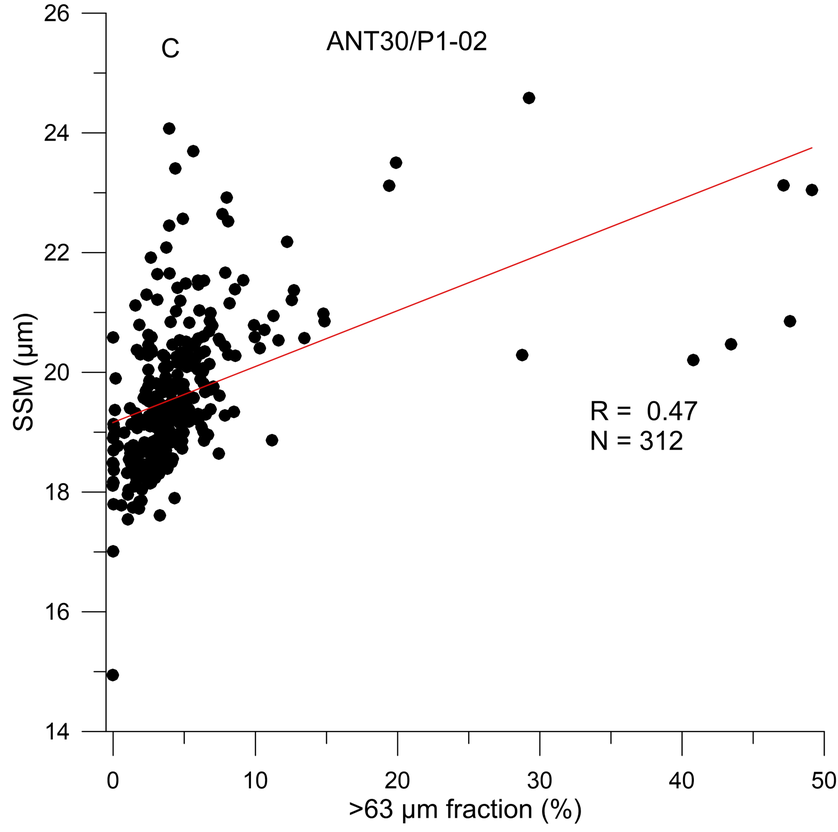
C
ANT30/P1-02
R = 0.47
N = 312
SSM (µm)
>63 µm fraction (%)

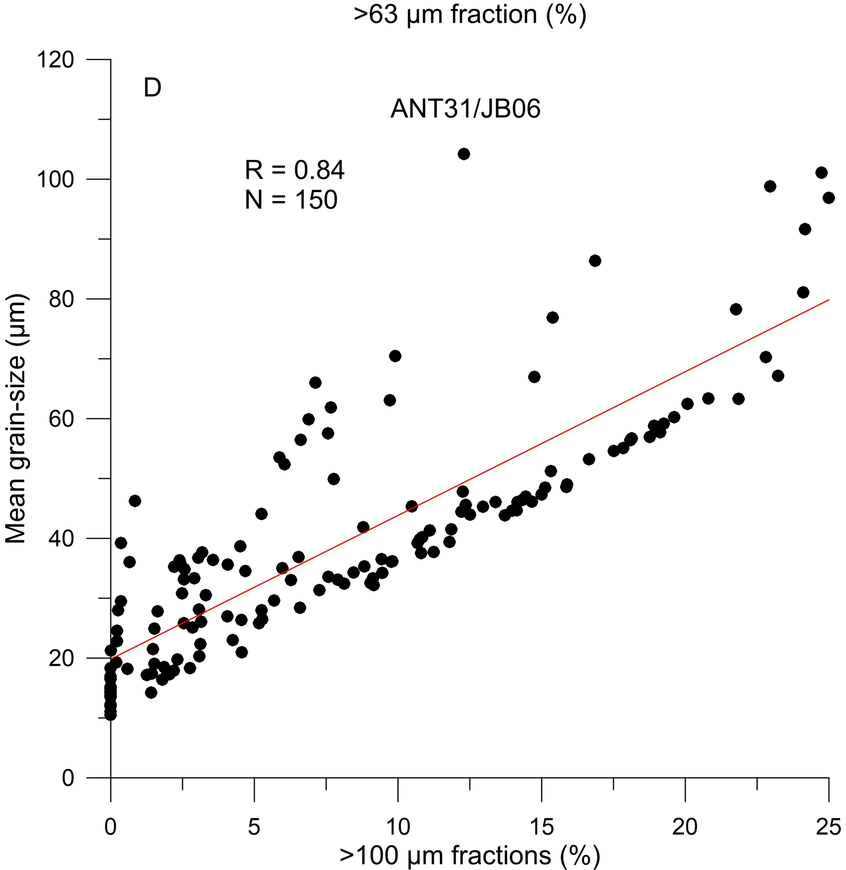
D
ANT31/JB06
R = 0.84
N = 150
Mean grain-size (µm)
>100 µm fractions (%)

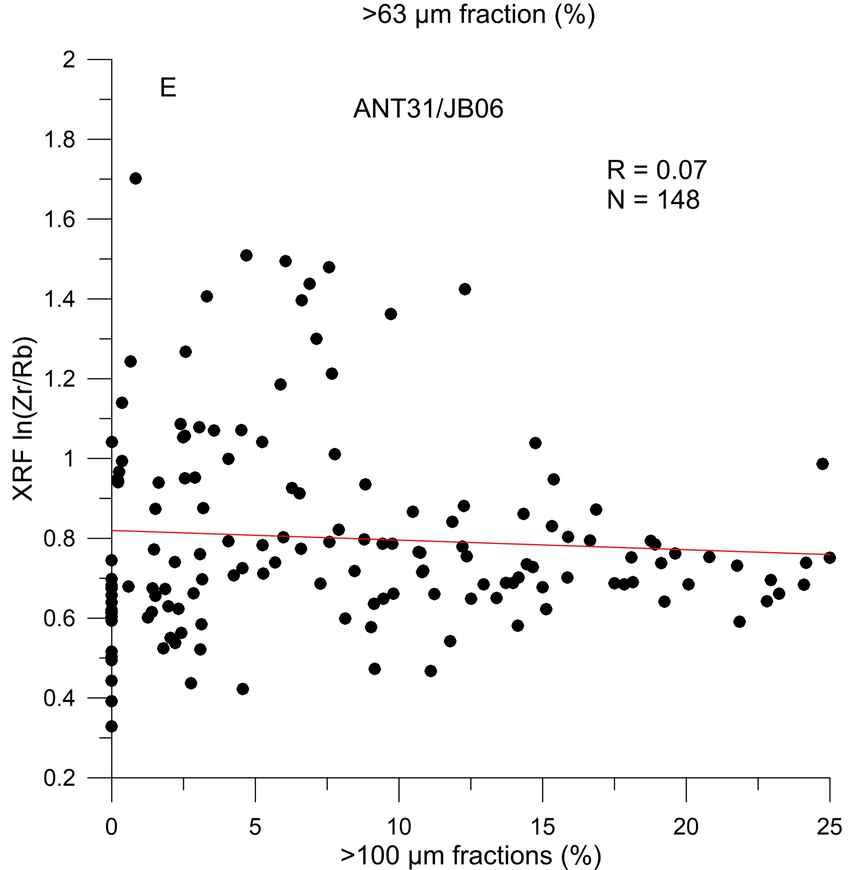
E
ANT31/JB06
R = 0.07
N = 148
XRF ln(Zr/Rb)
>100 µm fractions (%)

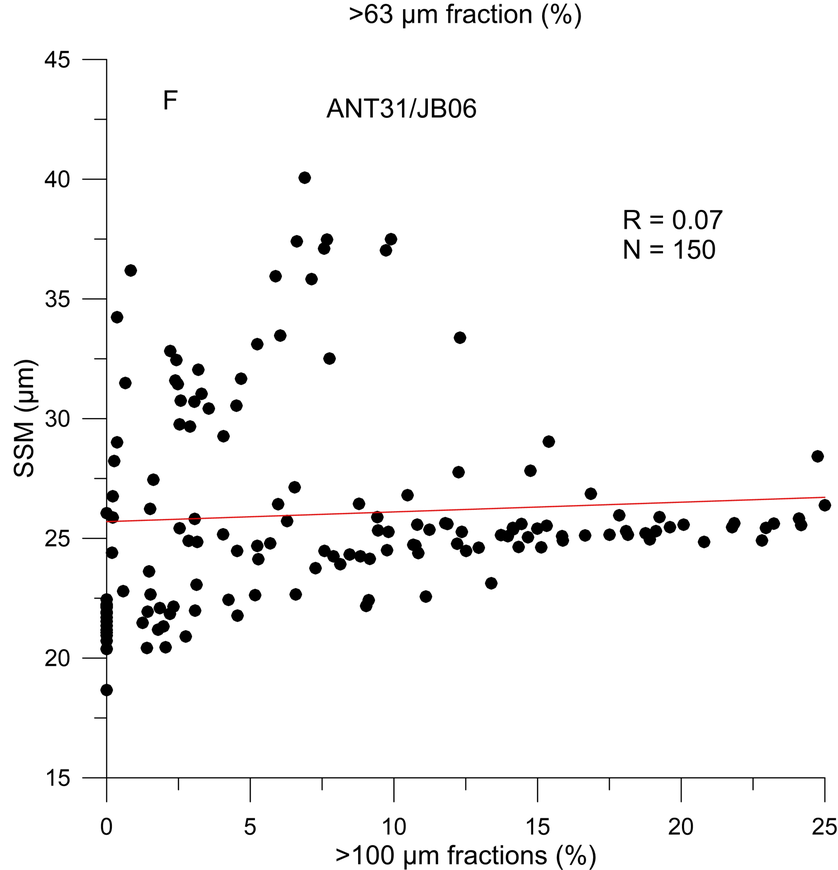
F
ANT31/JB06
R = 0.07
N = 150
SSM (µm)
>100 µm fractions (%)

Figure 10.

MIS 2 4 6 8 10 12

A

B

C

D

E

PMG_{63} (μm)

$Fractions_{7\text{-}63\ μm}/Fractions_{<6\ μm}$

SS% (%)

SSM (μm)

XRF ln(Zr/Rb)

Age (ka)

Figure 11.

A
B
C
D
E
PMG_{100} (µm)
$Fractions_{30-100\ µm}/Fractions_{<23\ µm}$
SS% (%)
SSM (µm)
XRF ln(Zr/Rb)
Depth (cm)

Figure 12.

A

P1-2
P1-2 S = 0.064, R = 0.37
JB06
JB06 S = 0.34, R = 0.86
3128
3128 S = 0.32, R = 0.83
93-2
93-2 S = 0.28, R = 0.88

SSM (μm)
SS% (%)

B

P1-2
P1-2 S = 38.3, R = 0.9
JB06
JB06 S = 32.6, R = 0.86
3128
3128 S = 34.4, R = 0.86
93-2
93-2 S = 28.4, R = 0.8

SS% (%)
XRF ln(Zr/Rb)

C

P1-2
P1-2 S = 1.37, R = 0.19
JB06
JB06 S = 14.1, R = 0.85
3128
3128 S = 12.7, R = 0.83
93-2
93-2 S = 9.67, R = 0.83

SSM (μm)
XRF ln(Zr/Rb)

D

P1-2
JB06
3128
93-2
All data except P1-2
S = 0.32, R = 0.85

SSM_N (μm)
$SS\%_N$ (%)

E

P1-2
JB06
3128
93-2
All data S = 34.1, R = 0.84

$SS\%_N$ (%)
XRF $ln(Zr/Rb)_N$

F

P1-2
JB06
3128
93-2
All data except P1-2
S = 12.7, R = 0.83

SSM_N (μm)
XRF $ln(Zr/Rb)_N$